
Application of the chiral forces to electroweak processes

Vitalii Urbanevych

Ph.D. thesis written under the supervision of dr. hab Roman Skibiński
at the Jagiellonian University, Faculty of Physics, Astronomy
and Applied Computer Science, Kraków,
Thursday 5th January, 2023



CONTENTS

1	Plan	2
2	Formalism & numerical methods	6
2.1	Deuteron bound state	6
2.2	2N scattering state	8
2.2.1	The Lippmann-Schwinger equation	8
2.3	3N bound state	10
2.4	Photodisintegration transition amplitude for Nd state	11
2.5	3N scattering state	12
2.6	Nuclear electromagnetic current	12
2.7	Theoretical uncertainties	12
3	Results	15
3.1	Deuteron photodisintegration	15
3.1.1	Cross section	15
3.1.2	Polarisation observables	21
3.2	Helium photodisintegration	35
3.2.1	3N photodisintegration	35
3.2.2	D-n photodisintegration	42
3.3	Pion absorption from the lowest atomic orbital	43
3.3.1	Pion absorption in ^3He	43
3.3.2	$\pi^- + ^3\text{H} \rightarrow n + n + n$	51
	Bibliography	55

CHAPTER 1

PLAN

- Why we study few nucleon systems
 - Strong interactions (2N and 3N force investigation; QCD, relativistic effects)
 - Electro-magnetic processes (electrons-, photons-induced reactions) (Arenhovel did ...)
 - Weak interactions (neutrons)
- Nuclear forces used in the thesis
 - AV18
 - Chiral (scs, sms; difference between chiral models; regularization problem)
- Currents used in the thesis (regularization of currents to be done)
- Formalism & numerical methods
 - Lippman-Schwinger eq
 - Schrodinger eq for deuteron; wave functions (sms) for deuteron - figures, binding energy
 - Three body: Fadeev eq. for bound (He3, H3) and scattering states
 - Siegert theorem ?
 - Partial wave decomposition, states ($pq\alpha$), Jakobi momenta; operators in PW decomp. (current); Mathematica for PW
 - Theoretical uncertainties: truncation error, cut-off dependency, chiral order dependency
- Results (**find everything what I have calculated: all processes and energies**)
 - H2 photodisintegration
 - He3 and H3 photodisintegration
 - Pion capture

- Summary
- References

Why we study few nucleon systems

The study of light nuclei and their reactions for the decades has been serving as an easiest way to investigate NN systems and forces inside the atoms. Convenient way to proceed may be an interaction of nucleus with other nucleus, particles or electromagnetic probes in elastic or inelastic scattering. It is possible to perform such an experiments and check if theory works. People take into account that interactions may be caused by different forces and therefore should be described in different ways. It can be either strong, weak or electromagnetic interaction. It depends on the type of particle being scattered and the target which reaction it is.

In order to proper describe the nuclear reactions many components should be taken into account. First of all, different forces may act on the participants.

The strong nuclear force appear inside the nuclei and among others bound neutrons and protons together. The description of strong interactions is extremely difficult as it deals not only with nucleon, but with their constituents: quarks and gluons. Quantum chromodynamics (QCD) is a modern theory describing strong interactions, but it has also its limitations and, at the moment, it is not useful at low energies ($Q^2 \lesssim 1\text{GeV}^2$). So other approaches are coming into the scene such as chiral effective theory, lattice calculation and others [1].

Starting the study of three- (and more) nucleon systems it was found that strong 2N force is not enough to describe the system and 3N force was introduced. The first applications of such a force showed that it brings sufficient contribution and cannot be ignored [2]. Whereas the first applications included only early "realistic" potential, the latter investigations only proved this statements [3, 4]. It was also used to construct four-nucleon (4N) bound state [5].

Electromagnetic force appears between charged particles like protons, electrons or pions. Also, the force is transferred between charged particles with a photon, so in photon- and electron- scatterings on the nuclei an electromagnetic force is playing an important role. Arenhövel [6] studied electromagnetic process - deuteron photodisintegration, applying different approaches and comparing the results with experimental data.

The weak force...

...

Nuclear forces used in the thesis

In order to construct a potential people often use phenomenological or semi-phenomenological approaches. It allows to combine theoretical knowledge about processes and experimental data.

One of such potentials, which was used in current thesis is Argonne V18 (AV18) [7] In order to construct NN force, authors combine analytical electromagnetic and one-pion-exchange parts with phenomenological one, fitting parameters to the Nijmegen partial-wave analysis of pp and np data [8]. Authors showed, that AV18 potential delivers good results in the description of nucleon scattering data as well as deuteron properties.

In the early 1990-ies Weinberg [9, 10] introduced an idea of using a most general Lagrangian satisfying assumed symmetry principles and in particular spontaneously broken

chiral symmetry to describe nuclear interactions at low energies. This idea together with effective field theory (EFT) of QCD led to the development of the Chiral Effective Field Theory (χ EFT) which nowadays has become one of the most advanced approach to describing nuclear reactions at low energies.

For the EFT it is very important to define a quantity, which powers will determine a perturbation order. In the χ EFT there are two natural scales: so-called soft scale - the mass of Pion $Q \sim M_\pi$ and hard scale - $\Lambda_\chi \sim 1 \text{ GeV}$ (chiral symmetry breaking scale). The ratio between these two scales $(Q/\Lambda_\chi)^\nu$ is being used as an expansion parameter in χ EFT with power ν .

Considering so-called irreducible (the diagrams that cannot be split by cutting nucleon lines), Weinberg [9, 10] came to the identity for the powers of such diagrams

$$\nu_W = 4 - A - 2C + 2L + \sum_i \Delta_i, \quad (1.1)$$

where

$$\Delta_i \equiv d_i + \frac{n_i}{2} - 2 \quad (1.2)$$

In Eq. (1.1), C is a number of pieces which are connected, L - the number of loops in the graph. In Eq. (1.2), n_i is a number of nucleon field operators, d_i - the number of insertions (or derivatives) of M_π .

The further analysis of Eq. (1.1) revealed some problems which occur for particular values of parameters in the equation, namely negative values of ν_W are possible. In order to deal with that, Eq. (1.1) was slightly modified adding $3A - 6$ to it [11, 12]:

$$\nu = \nu_W + 3A - 6 = -2 + 2A - 2C + 2L + \sum_i \Delta_i \quad (1.3)$$

In χ EFT the first order is called "leading order" (LO, $\nu = 0$) and it is followed by next-to-leading order (NLO, $\nu = 2$)¹, next-to-next-to-leading order (N²LO, $\nu = 3$) and so on. At each chiral order, particular interaction diagrams are described. At LO there is a diagram which consists of 2 contact terms and the diagram implying one-pion exchange. Both diagrams reflect only 2NF as well as diagrams at NLO, where more contact terms are introduced together with two-pion exchange diagrams. Each subsequent order includes more and more sophisticated diagrams describing nucleons interaction, 3NF appears at N²LO while 4NF contributions are firstly described at N³LO. So there is a systematic way to include all the forces from simplest diagrams at LO and gradually adding more and more terms. It is also beneficial in the way that one can obtain results using chiral potential at different orders and track which one gives larger or smaller contribution (changes in the final results). The highest order for which there is a derived term in potential is N⁴LO at the moment. Nevertheless leading F-wave contact interactions from N⁵LO are included in the N⁴LO+ potential, which is regarded as a best possible potential within my work.

There are a number of another approaches within χ EFT utilized. The group of Piarulli is using quite similar approach, including the same chiral potentials with minor differences [13, 14].

Machleidt, Ekstrim, pion-less EFT, Lattice EFT(Mesissner)

¹The $\nu = 1$ order is completely vanished due to parity and time-reversal invariance, so next-to-leading order stands for the second order of expansion.

The χ EFT may be applied both in coordinate and momentum spaces. Nevertheless in both cases it requires regularization which is cutting low coordinate values in order to avoid infinities (or high momentum values - in momentum space). The semilocal momentum-space regularized (SMS) potential is being regularized using the Gaussian form factor $F(\vec{l}^2)$:

$$F(\vec{l}^2) = e^{-\frac{\vec{l}^2 + M_\pi^2}{\Lambda^2}}, \quad (1.4)$$

where M_π is an effective pion mass and Λ - is a cutoff parameter.

The form factor from Eq. (1.4), being used together with Feynman propagator, ensures that long-range part of the forces has no singularities.

The value at which the cut is applied (cut-off value) is not fixed and usually calculations are being performed for different cut-off values. The comparison of such results may reveal stronger or weaker dependance and in perfect case one will come up with such a potential, were the cut will not affect results much. On the Fig. 1.1 I show values of the 2N potential $\langle \vec{p} | V | \vec{p}' \rangle$ as a function on the momentum $|\vec{p}'|$ with fixed value $|\vec{p}| = 0.054 \text{ [fm]}$.

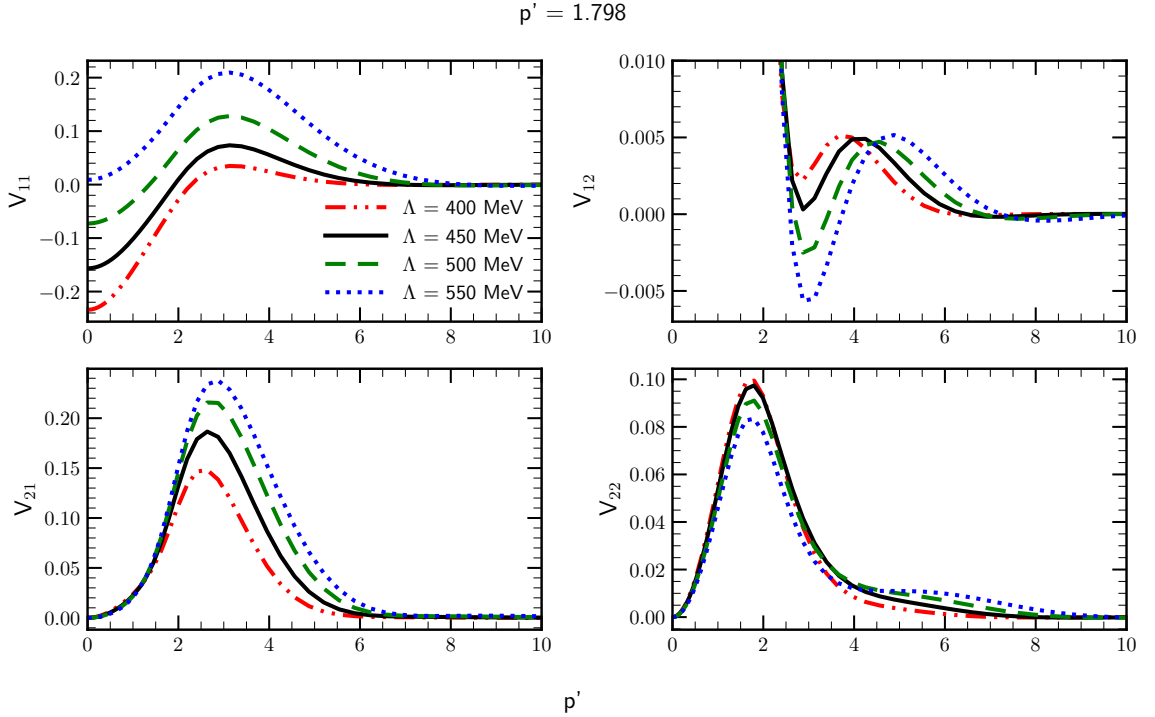


Figure 1.1: Potential components as a function on the momentum p with fixed value of the momentum $p' = 1.798 \text{ [fm]}$.

The potential may be transformed from coordinate to momentum space (or vice versa), but it is important at which frame the regularization was performed and what was a regularization function. That's why there are different versions of chiral potential. One is semilocal coordinate-space regularized (SCS) potential [15] and another one is similar, but with regularization applied in momentum space (SMS potential) [16].

Currents

CHAPTER 2

FORMALISM & NUMERICAL METHODS

Despite the deuteron problem was solved long time ago, I will describe it briefly in order to introduce the notation and formalism. For 3N case only extension will be needed.

In order to calculate any observable for the deuteron photodisintegration, one has to find a nuclear matrix elements:

$$N^\mu = \langle \Psi_f \vec{P}_f | \frac{1}{e} J^\mu(0) | \Psi_i \vec{P}_i \rangle = \langle p'(l's')j'm'_jt'm'_t \vec{P}_f | J^\mu | \phi_d m_d \vec{P}_i \rangle, \quad (2.1)$$

where J^μ is a four-vector current operator which acts between initial and final two-nucleon states.

2.1 Deuteron bound state

Let's find a deuteron bound state wave function ϕ_d . The time-independent Schrödinger equation for two particles in such case will be:

$$(H_0 + V) | \psi_{12} \rangle = E_d | \psi_{12} \rangle, \quad (2.2)$$

with a kinetic energy H_0 and potential V . The kinetic energy H_0 can be represented in terms of relative and total momenta of the particles:

$$H_0 = \frac{\vec{p}_1^2}{2m_1} + \frac{\vec{p}_2^2}{2m_2} = \frac{\vec{p}^2}{2\mu} + \frac{\vec{P}^2}{2M}, \quad (2.3)$$

where relative and total momenta are defined as follows:

$$\vec{p} = \frac{(m_1 \vec{p}_1 - m_2 \vec{p}_2)}{m_1 + m_2} \quad (2.4)$$

$$\vec{P} = \vec{p}_1 + \vec{p}_2 \quad (2.5)$$

and $M = m_1 + m_2$ is a total mass, $\mu = \frac{m_1 m_2}{M}$ is a relative mass of two nucleons, \vec{p}_i is a momentum of i-th particle.

Potential V is assumed to depend on the relative degrees of freedom, so Eq. (2.2) may be decomposed into two separated equations:

$$\frac{\vec{p}^2}{2\mu} \langle \vec{p} | \Psi_{int} \rangle + \int d\vec{p}' \langle \vec{p} | V | \vec{p}' \rangle \langle \vec{p}' | \Psi_{int} \rangle = (E_d - E_{c.m.}) \langle \vec{p} | \Psi_{int} \rangle \quad (2.6)$$

$$\frac{\vec{P}^2}{2M} \langle \mathcal{P} | \Psi_{c.m.} \rangle = E_{c.m.} \langle \mathcal{P} | \Psi_{c.m.} \rangle, \quad (2.7)$$

with $\langle \vec{p}, \vec{\mathcal{P}} | H_0 | \Psi_{12} \rangle = \frac{\vec{p}^2}{2\mu} \langle \vec{p} | \Psi_{int} \rangle + \frac{\vec{P}^2}{2M} \langle \mathcal{P} | \Psi_{c.m.} \rangle$. So $\Psi_{c.m.}$ is a component of total wave function, which reflects a deuteron as a single object with momentum $\vec{\mathcal{P}}$ while Ψ_{int} is an internal wave function describing interaction between nucleons. Basis state $|\vec{p}\rangle$ obeys a completeness equation:

$$\int d^3\vec{p} |\vec{p}\rangle \langle \vec{p}| = \mathbb{1} \quad (2.8)$$

Eq.(2.6) is basically a Schrödinger equation for one particle with mass μ and Eq.(2.7) can be regarded as a Schrödinger equation for particle with mass M in a free motion. Assuming that deuteron is at rest ($E_{c.m.} = 0$) we can stick to the Eq.(2.6) only. So that:

$$\frac{\vec{p}^2}{2\mu} \langle \vec{p} | \Psi_{int} \rangle + \int d\vec{p}' \langle \vec{p} | V | \vec{p}' \rangle \langle \vec{p}' | \Psi_{int} \rangle = E_d \langle \vec{p} | \Psi_{int} \rangle \quad (2.9)$$

Working in 3 dimensional space is difficult (especially numerically) so i introduce the partial-wave representation (PWD) of the momentum state in the following form:

$$|\vec{p}\rangle = |p\alpha\rangle \equiv |p(ls)jm_j\rangle |tm_t\rangle, \quad (2.10)$$

where we introduce quantum numbers l, s, j, t as orbital angular momentum, total spin, total angular momentum and total isospin respectively. m_j and m_t are isospin and spin projections.

Yet one can introduce simpler states than it is in (2.10).

$$|p(ls)jm_j\rangle = \sum_{m_l} c(ls j; m_l, m_j - m_l, m_j) |plm_l\rangle |s m_j - m_l\rangle \quad (2.11)$$

Also we can decompose spin and isospin states as follows:

$$|sm_s\rangle = \sum_{m_1} c(\frac{1}{2} \frac{1}{2} s; m_1, m_s - m_1, m_s) |\frac{1}{2} m_1\rangle |\frac{1}{2} m_s - m_1\rangle \quad (2.12)$$

$$|tm_t\rangle = \sum_{\nu_1} c(\frac{1}{2} \frac{1}{2} t; \nu_1, m_t - \nu_1, m_t) |\frac{1}{2} \nu_1\rangle |\frac{1}{2} m_t - \nu_1\rangle \quad (2.13)$$

In Eqs.(2.11) -(2.13), $c(\dots)$ are Clebsh-Gordon coefficients. Nucleons are spin $\frac{1}{2}$ particles, and also we treat proton and neutron as the same particle in different isospin states, so that isospin is $\nu_1 = \frac{1}{2}$ for proton and $\nu_1 = -\frac{1}{2}$ for neutron.

The states $|plm_l\rangle$ from Eq.(2.11) are orthogonal, so that

$$\langle p'l'm'_l | plm_l \rangle = \frac{\delta(p - p')}{p^2} \delta_{ll'} \delta_{m_l m'_l} \quad (2.14)$$

and also satisfy the completeness relation:

$$\sum_{l=0}^{\infty} \sum_{m_l=-l}^l \int dp p^2 |plm_l\rangle \langle plm_l| = \mathbb{1} \quad (2.15)$$

These states also fulfill a relation

$$\langle \vec{p}' | plm_l \rangle = \frac{\delta(|\vec{p}'| - p)}{p^2} Y_{lm_l}(\hat{p}'), \quad (2.16)$$

where $Y_{lm_l}(\hat{p}')$ is a spherical harmonic and ' $\hat{\cdot}$ ' means a unit vector in direction of \vec{p} :

$$\vec{p} \equiv |\vec{p}| \hat{p} \equiv p \hat{p} \quad (2.17)$$

Nucleons are fermions so exchanging leads to antisymmetry of the wave function. In PWD it leads to the requirement which can be expressed as:

$$(-1)^{l+s+t} = -1 \quad (2.18)$$

Taking into account Eq.(2.18), one can find only one possible PWD state combination for the deuteron bound state (under ... experimental evidence): 2 coupled channels for $l=0,2$; $s=1$; $j=1$ and $t = m_t = 0$. These 2 channels are usually denoted as 3S_1 and 3D_1 and corresponding wave functions are $\phi_0(p)$ and $\phi_2(p)$:

$$\phi_l(p) = \langle pl | \Psi_{int} \rangle = \langle p(l1)1m_d | \langle 00 | \Psi_{int} \rangle ; l = 0, 2. \quad (2.19)$$

So with a new basis Eq.(2.9) takes a form:

$$\frac{\vec{p}^2}{2\mu} \phi_l(p) + \sum_{l'=0,2} \int dp' p'^2 \langle plm_l | V | p'l'm'_l \rangle \phi_{l'}(p) = E_d \phi_l(p), \quad (2.20)$$

for $l = 0, 2$. In case one does not have a matrix elements for the potential $\langle plm_l | V | p'l'm'_l \rangle$ in analytical form, but only values for some grid of points, there is still one complication in the Eq.(2.20) - integration. In order to get rid of the integral I use a Gaussian quadrature method of numerical integration [17]. It allows to replace an integral by the weighted sum: $\int_a^b f(x) dx = \sum_{i=1}^n \omega_i f(x_i)$ In current work I used 72 points in the interval from 0 to $50fm$. Using this method, Eq.(2.9) becomes

$$\frac{\vec{p}^2}{2\mu} \phi_l(p) + \sum_{l'=0,2} \sum_{j=0}^N \omega_j p_j'^2 \langle p_j l m_l | V | p_j' l' m'_l \rangle \phi_{l'}(p) = E_d \phi_l(p), \quad (2.21)$$

I solve this equation as an eigenvalue problem $M\Psi = E_n\Psi$ and in that way find simultaneously wave function values and binding energy E_n . The binding energy E_n calculated with potentials of different chiral orders is presented on the Fig. 2.1.

2.2 2N scattering state

2.2.1 The Lippmann-Schwinger equation

Let us start from the time-independent formulation of the scattering process. In such a case Hamiltonian will be:



Figure 2.1: Deuteron binding energy calculated using chiral potential with different chiral orders. Error bands represent a standard deviation of the calculated binding energy with respect to the cutoff parameter Λ . Experimental data is taken from [18]

$$H = H_0 + V, \quad (2.22)$$

where H_0 is a kinetic energy operator $H_0 = \frac{\vec{p}^2}{2m}$ and V is a nucleon-nucleon interaction. For a free particle motion, V will be absent and we will denote an energy eigenstate as $|\vec{p}\rangle$ - a free particle state. In the case of the scattering process, the eigenstate will differ from $|\phi\rangle$, but in case of elastic scattering (which we are interested in) the energy eigenvalue E should be the same.

So these two states fulfill Schrödinger equations for such scattering process:

$$\begin{cases} H_0 |\vec{p}\rangle &= E |\vec{p}\rangle \\ (H_0 + V) |\psi\rangle &= E |\psi\rangle \end{cases} \quad (2.23)$$

We are interested in solution for Eq. (2.23), so that $|\psi\rangle \rightarrow |\vec{p}\rangle$ as $V \rightarrow 0$ and both $|\psi\rangle$ and $|\vec{p}\rangle$ have the same energy eigenvalues E . As we have scattering process, the energy spectra for both operators H_0 and $H_0 + V$ are continuous.

From Eq. (2.23) follows that

$$|\psi\rangle = \frac{1}{E - H_0} V |\psi\rangle + |\vec{p}\rangle, \quad (2.24)$$

where $|\vec{p}\rangle$ is a solution to the free-particle Schrödinger equation

$$H_0 |\vec{p}\rangle = E |\vec{p}\rangle, \quad (2.25)$$

with same energy eigenvalue [19]. In addition, it guarantees that application of the operator $(E - H_0)$ to the (2.24) results in the second equation from the system (2.23).

In order to deal with a singular operator $\frac{1}{E - H_0}$ in eq.(2.24), the well-known technique is to make such an operator complex by adding small imaginary number to the denominator so Eq.(2.24) becomes

$$|\psi\rangle = G_0(E \pm i\epsilon)V |\psi\rangle + |\vec{p}\rangle, \quad (2.26)$$

where G_0 is a free propagator:

$$G_0(z) = \frac{1}{z - H_0} \quad (2.27)$$

Solution with $G_0(E - i\epsilon)$ corresponds to the incoming spherical wave, while $G_0(E + i\epsilon)$ - to the outgoing one. Since we are interested in the scattering process, only the (+) sign survives.

Eq. (2.26) is known as a Lippmann-Schwinger equation (LSE) and using the definition of the transition operator t :

$$t|\vec{p}\rangle = V|\psi\rangle \quad (2.28)$$

we can rewrite it as

$$|\psi\rangle = (1 + G_0(E + i\epsilon)Vt)|\vec{p}\rangle \quad (2.29)$$

With substitution of Eq. (2.26) into Eq. (2.28) we can find an explicit form of the t operator:

$$\begin{aligned} t|\vec{p}\rangle &= VG_0(E + i\epsilon)V|\psi\rangle + V|\vec{p}\rangle = \\ &= VG_0(E + i\epsilon)t|\vec{p}\rangle + V|\vec{p}\rangle \end{aligned} \quad (2.30)$$

Getting rid of the initial state $|\vec{p}\rangle$ in the Eq. (2.30) we can get a LSE for the transition operator in the iterative form:

$$\begin{aligned} t &= V + VG_0Vt = \\ &= V + VG_0V + VG_0VG_0V + \dots \end{aligned} \quad (2.31)$$

In the partial-wave representation, LSE Eq. (2.30) may be written as:

$$\begin{aligned} \langle p'(l's')jt|t(E)|p(ls)jt\rangle &= \langle p'(l's')jt|V|p(ls)jt\rangle + \\ &+ \sum_{l''} \int_0^\infty dp'' p''^2 \langle p'(l's')jt|V|p''(l''s)jt\rangle \\ &\times \frac{1}{E + i\epsilon - p''^2/m} \langle p''(l''s)jt|t(E)|p''(ls)jt\rangle \end{aligned} \quad (2.32)$$

Using Eq. (2.29) we can write Eq. (2.1) as

$$N^\mu = \langle \phi m_p m_n | (1 + G_0(E + i\epsilon)Vt) \frac{1}{e} J^\mu(0) | \Psi_i \vec{P}_i \rangle \quad (2.33)$$

2.3 3N bound state

The 3N bound state is derived from a general Schrödinger for 3N system and its total wave function obeys the following equation:

$$|\Psi_i\rangle = G_0(E + i\epsilon) \sum_{j=1}^3 (V_j + V_4^j) |\Psi_i\rangle, \quad (2.34)$$

where G_0 is a free propagator from Eq. (2.27), V_j - is a two-body potential acting between nucleons k and l (j, k and l - are the numbers of each nucleon) and V_4^j is a component of three-body potential $V_4 = \sum_{j=1}^3 V_4^j$. E - is a binding energy.

Eq. (2.34) can be split into 3 independent equations for so-called Faddeev components $|\psi_j\rangle$

$$|\Psi_i\rangle = \sum_{j=1}^3 |\psi_j\rangle. \quad (2.35)$$

Using Eq. (2.35) one can decompose Eq. (2.34) into separate equations for each Faddeev component:

$$|\psi_j\rangle = G_0(E + i\epsilon)(V_j + V_4^j) |\Psi_i\rangle, \quad (2.36)$$

Next I introduce a permutation operator P , which is a combination of operators P_{jk} :

$$P = P_{12}P_{23} + P_{13}P_{32}. \quad (2.37)$$

The operator component P_{jk} acting on the state interchange the momenta and quantum numbers of the nucleon number j and k .

Using Eq. (2.37) and Eq. (2.35), one can rewrite Eq. (2.36) in the following form:

$$|\psi_j\rangle = G_0(E + i\epsilon)t_j P |\psi_i\rangle + (1 + G_0(E + i\epsilon)t_j)G_0(E + i\epsilon)V_4^j(1 + P) |\psi_i\rangle, \quad (2.38)$$

where t_j is a two-body t -operator which obeys Eq. (2.30) for corresponding two-body potential V_j .

2.4 Photodisintegration transition amplitude for Nd state

Analogously to the bound state, one can express a nucleon-deuteron scattering state using a permutation operator Eq. (2.37).

$$|\Psi^{(-)}\rangle^{Nd} = \frac{1}{\sqrt{3}}(1 + P) |\Psi_1^{(-)}\rangle^{Nd} \quad (2.39)$$

A scattering state $|\Psi_1^{(-)}\rangle^{Nd}$ can be expressed in terms of asymptotic state $|\Phi_1^{Nd}\rangle$, where particles 2 and 3 form a deuteron and the third particle (number 1) is a nucleon which propagates freely with relativemomentum \vec{q}_0 with respect to the deuteron:

$$|\Psi_1^{(-)}\rangle^{Nd} \equiv \lim_{\epsilon \rightarrow 0} i\epsilon G(E_{Nd} - i\epsilon) |\Phi_1^{Nd}\rangle \quad (2.40)$$

$$|\Phi_1^{Nd}\rangle \equiv |\Phi_{d(2,3)}\rangle |\vec{q}_0\rangle, \quad (2.41)$$

where $|\Phi_{d(2,3)}\rangle$ is a deuteron wave function and $|\vec{q}_0\rangle$ - a free particle state. E_{Nd} is a total energy of the 3N system:

$$E_{Nd} = E_d + \frac{3|\vec{q}_0|^2}{4m}, \quad (2.42)$$

where E_d is a deuteron binding energy and m - nucleon mass.

The full propagator $G(E_{Nd})$ in this case takes a form:

$$G(z) = \frac{1}{z - (H_0 + \sum_{i=1}^4 V_i)} \quad (2.43)$$

2.5 3N scattering state

As in Sec. 2.4, one can write an equation for the 3-nucleone scattering state:

$$|\Psi^{(-)}\rangle^{3N} = \frac{1}{\sqrt{3}} |\Psi_j^{(-)}\rangle^{3N} \quad (2.44)$$

with a set of corresponding equations for $|\Psi_j^{(-)}\rangle^{3N}$

$$|\Psi_j^{(-)}\rangle^{3N} \equiv \lim_{\epsilon \rightarrow 0} i\epsilon G(E_{3N} - i\epsilon) |\Phi_j^{3N}\rangle \quad (2.45)$$

$$|\Phi_j^{3N}\rangle \equiv \frac{1}{\sqrt{2}} (1 - P_{kl}) |\vec{p}(kl)\vec{q}(j)\rangle \quad (2.46)$$

$$E_{3N} = \frac{|\vec{p}|^2}{m} + \frac{3|\vec{q}|^2}{4m}, \quad (2.47)$$

2.6 Nuclear electromagnetic current

2.7 Theoretical uncertainties

Truncation error

As it was mention above, each subsequent order of chiral expansion provides us with more and more sophisticated potential which is expected to increase accuracy of data description. Starting from the leading order (LO) and coming next to N2LO, N3LO and so on, we take into account more Feynmann diagrams and in result potential is expected to provide us with more precise predictions for the regarded process and observable. But the chiral expansion (as any expansion) in principle can be continued up to the infinity, improving the resulting series. In practice we are limited by a finite, rather small, number of terms and we would like to find out the uncertainty appearing from cutting off remaining part of the expansion. This theoretical uncertainty is called a truncation error. Various ways of estimation its value have been proposed [20–24]. Such estimation is based on predictions at lower orders. It is worth adding that Bayesian analysis is also used for truncation error estimation

We use method proposed in [22]. Let's regard some observable $X^i(p)$ which is calculated at i -s order of chiral expansion with expansion parameter Q ($i = 0, 2, 3, \dots$)¹. Here

¹We do not have a first order of expansion because this term in chiral expansion is always vanished

p specifies a momentum scale of the current reaction in the center of mass frame (in the case of deuteron photodisintegration it would be a photon's momentum).

If I define a difference between observable at each subsequent orders as:

$$\Delta X^{(2)} = |X^{(2)} - X^{(0)}|, \Delta X^{(i>2)} = |X^{(i)} - X^{(i-1)}|, \quad (2.48)$$

then chiral expansion for X can be written as:

$$X = X^{(0)} + \Delta X^{(2)} + \Delta X^{(3)} + \dots + \Delta X^{(i)}. \quad (2.49)$$

The truncation error at order i - $\delta X^{(i)}$ - is estimated using actual and expected values of the observable at higher orders as following:

$$\delta X^{(0)} = Q^2 |X^{(0)}|, \quad (2.50)$$

$$\delta X^{(i)} = \max_{2 \leq j \leq i} (Q^{i+1} |X^{(0)}|, Q^{i+1-j} |\Delta X^{(j)}|). \quad (2.51)$$

Additionally, following the [22] I use the actual high-order predictions in order to specify uncertainties so that:

$$\delta X^{(i)} \geq \max_{j,k} (|X^{j \geq i} - X^{k \geq i}|) \quad (2.52)$$

and to be conservative I use additional restriction:

$$\delta X^{(i)} \geq Q \delta X^{(i-1)}. \quad (2.53)$$

All the conditions above assume that we use the whole available information at hand.

Cutoff dependency

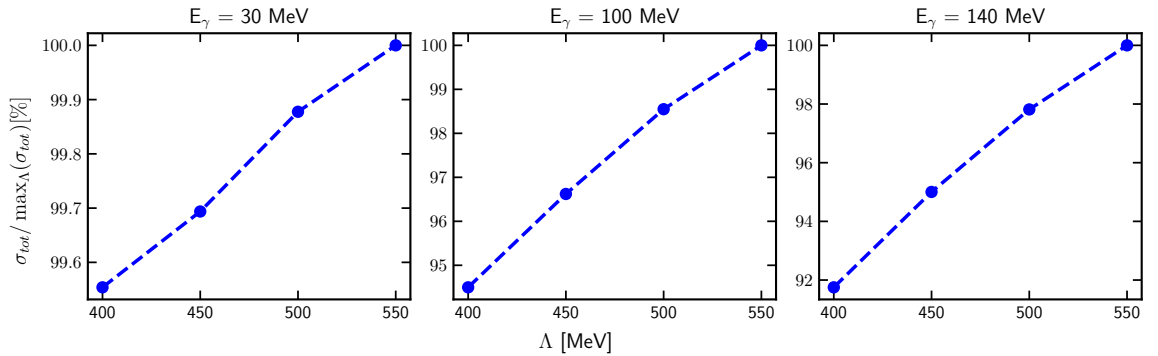


Figure 2.2: Total cross section of the deuteron photodisintegration process (normalized to the maximal cross section among all Λ) as a dependence on the cutoff parameter Λ for three photon energy E_γ values: 30, 100 and 140 MeV.

Another theoretical uncertainty comes from the choice of the cutoff parameter's value which was mentioned already.

and NLO corresponds to the quadratic term (number 2)

According to [16], where the SMS potential was presented, four values of the cutoff parameter Λ are recommended: 400, 450, 500 and 550 MeV. Using each of them one obtains different predictions which off course can further differ from actual (experimental) value. Therefore the choice of Λ value may affect a quality of the prediction.

Comparison of predictions obtained with different values of the cutoff parameter Λ is presented on the Fig. 2.2. Each subfigure shows a predictions for the total cross section as a function of the cutoff parameter for the photons energies 30, 100 and 140 MeV normalized to the maximum value among all cross sections obtained with various Λ (at the chiral order N^4LO+). As we can see, there is almost linear dependance with positive linearity coefficient value: with higher Λ the cross section value increases as well. The noticeable is also the fact, that with higher photon's energy, the cutoff dependance becomes stronger: for $E_\gamma = 30$ MeV the maximal difference between predictions is around 0.5% while for 140 MeV it increases to more than 8%. This results are generally within our expectations that our model works better at smaller energies.

Other uncertainties

There are a plenty possibilities where uncertainties may appear. Taking into account that all the results include calculations, we can come up with a lot of places where numerical methods with limited precision come into the scene. First of all we have a potential which is being defined on some grid of points. So the choice of grid affect a final results' precision. The same grid is also used for numerical integration (e.g. in Eq. (2.21)) where the final integral is also dependant on the points. Usually, we use a grid ...values

In addition our approach is based on the partial wave decomposition which supposes that limited number of partial waves are included (usually for 2N scattering we use $J^{max} = 4$ which corresponds to 18 partial waves).

Finally every computer calculations include limited machine precision which can be noticeable for a complex calculations.

CHAPTER 3

RESULTS

3.1 Deuteron photodisintegration

3.1.1 Cross section

In this section I will show the results of my calculation starting from the deuteron photodisintegration process. One of the most studying observable is obviously the cross section. There is a number of papers which present measurement results for both differential and total cross section [25–33] and it seems interesting to compare our predictions with experimental results.

In Fig. 3.1 and Fig. 3.2 I present predictions for the total cross section σ_{tot} [μb] which I obtained using the chiral potential at the order $\text{N}^4\text{LO}+$ and with the cutoff parameter $\Lambda = 450$ MeV (my best predictions). From Fig. 3.1, we see that at low photon energies (below 50 MeV) predictions which include 2N contributions via the Siegert approach, describe experimental results quite well. We can suppose that the difference with experimental data may come from the statistical uncertainty of the data itself, as my predictions are often in between the data from different sources. Moreover even at such low energies the 1N current is clearly not enough to describe this observable as dashed pink line has much lower values and the difference becomes even larger with larger photon's energies. At 5 MeV the difference between 1N predictions and 1N + Siegert is $297.54 \mu\text{b}$ (10.8%), increasing energy to 10 MeV it is $304.28 \mu\text{b}$ (20.4%) and at 20 MeV it is $229.50 \mu\text{b}$ (39.2%). Even with energy increasing from 5 MeV to 20 MeV - the difference between predictions has changed from 10.8% to 39.2% and from Fig. 3.1 we see that the gap continues increasing even more with larger energies.

Here and later the relative difference between set of predictions (x_1, x_2, \dots, x_N) is calculated using the formula:

$$\Delta = \frac{\max(x) - \min(x)}{\frac{1}{N} \sum_{i=1}^N x_i} \cdot 100\% \quad (3.1)$$

Having look at the higher energies (above 50 MeV, Fig. 3.2) we can notice that the discrepancy with experimental data is not only quantitative, but also qualitative. There is a peak around 300 MeV in the experimental data from [30] which is not reflected in my predictions. The reason of such discrepancy is most likely coming from the relativistic effects which I do not take into account. At higher energies their contribution becomes

larger and here we observe a clear justification of such a lack. It is also confirmed by the calculations in [6] where authors discuss different potentials applying to the Deuteron photodisintegration. Despite authors use a simpler potentials than ours, their predictions obtained with and without including relativistic effects show, that such a peak appears in the latter case.

Nevertheless my main goal is to describe deuteron photodisintegration at low energies and predictions seem to be well describing experimental data at $E_\gamma \lesssim 50$ MeV. The higher energies region is presented in order to investigate how far the predictions are from experimental results and what can be improved in the future (e.g. include relativistic part).

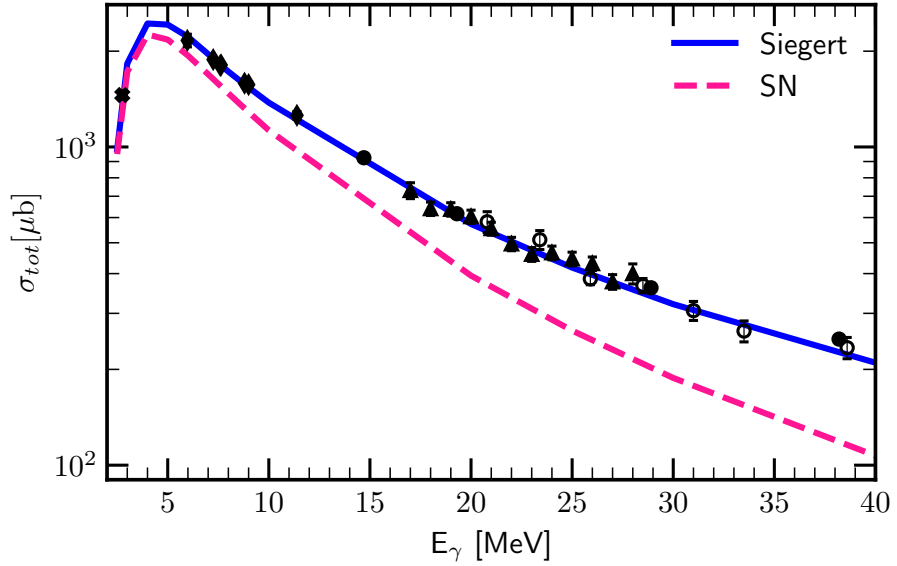


Figure 3.1: Total cross section as a function of the photon's energy E_γ . Solid blue line presents results obtained with SN+Siegert and dashed pink line - with only SN current. The experimental data are from [30] (black filled circles), [25] (empty circles), [26] (squares), [27] (triangles), [28] (cross "X") and [29] (diamonds).

In Fig. 3.3 I present an example of such a procedure being applied to the total cross-section for the deuteron photodisintegration at three photon energy values: 30, 100 and 140 MeV as a function of the chiral order. Error bands show truncation errors calculated using Eq. 2.50 - 2.53. One can see that truncation errors are being reduced with each consecutive chiral order: for LO it is the biggest while for N⁴LO+ it is hardly visible at presented scale. In each case the prediction is within the uncertainty range of lower orders.

Figures 3.4a - 3.5 show my predictions for the differential cross section $\frac{d\sigma}{d\Omega}$, where each subfigure presents results obtained using different values of the photon energy: 30, 100 and 140 MeV with 2N current's contributions taken into account via Siegert theorem. Fig. 3.4a shows the predictions obtained using different chiral orders (from LO to N⁴LO+) and with $\Lambda = 450$ MeV. Comparing the best predictions (N⁴LO+, $\Lambda = 450$ MeV) for each subfigure, we can conclude that the higher photon's energy is, the larger is difference between the theoretical predictions and experimental measurements. At $E_\gamma = 30$ MeV (top panel) my predictions almost perfectly match the data and the difference is almost always within the experimental uncertainties. Going to the energy 100 MeV (middle

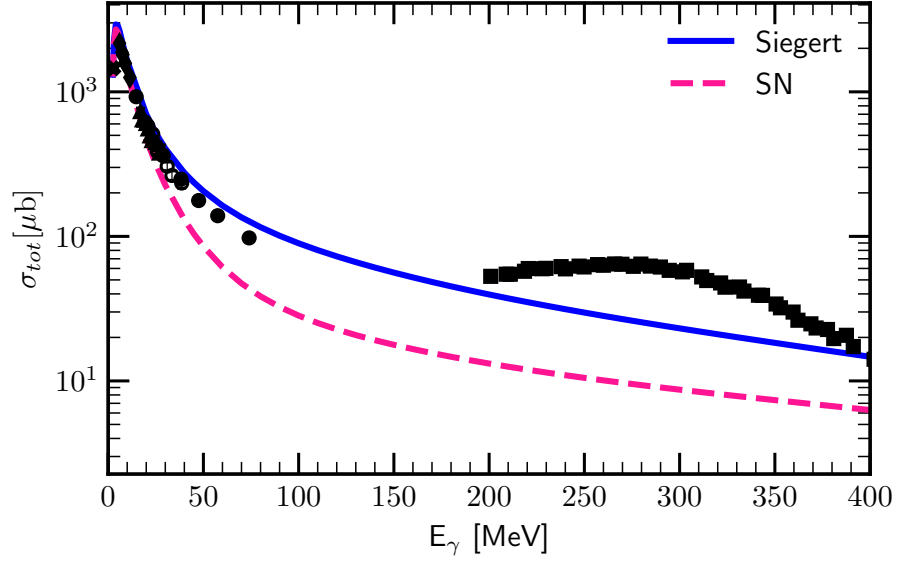


Figure 3.2: The same as on the Fig. 3.2 but for the energy range 2.5 - 400 MeV.

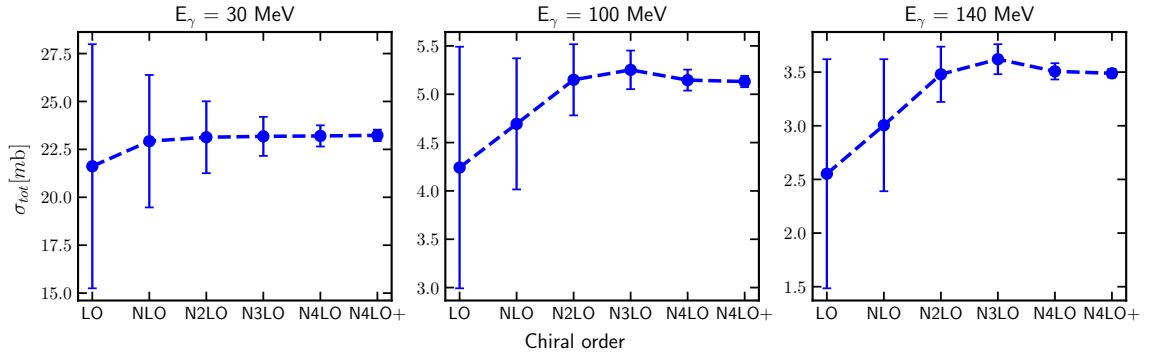


Figure 3.3: Total cross section of the deuteron photodisintegration process as a dependence on the chiral order for three photon energy E_γ values: 30, 100 and 140 MeV. Error bands show an estimated truncation error at each order.

subfigure) the descriptions seems not to be such good: theoretical predictions match the data qualitatively, but the gap in the angles range ($60^\circ < \theta_p < 130^\circ$) is around 30 % (check the value!). Looking at the bottom figure, it is even hard to say about good qualitative description: the general trend of the angular dependence is presented, but still the predictions are far from the experimental values.

Figures for each energy confirm the convergence of the predictions with respect to the chiral order. We see that the curves at LO are far from both experimental data and the best potential's predictions (N⁴LO+) and the higher is photon's energy, the larger is this difference. With each subsequent chiral order, the curves are more closer to each other and the difference between N⁴LO and N⁴LO+ is hardly visible at current scale. The relative difference at 30 MeV around the point of maximum ($\theta_p = 80^\circ$) is 0.05 % which is $0.02 \frac{\mu\text{b}}{\text{sr}}$; at 100 MeV and $\theta_p = 107^\circ$ it is 0.79 % ($0.025 \frac{\mu\text{b}}{\text{sr}}$); and at 140 MeV (same angle) it is 1.80% - $0.043 \frac{\mu\text{b}}{\text{sr}}$. Having such a small differences between predictions from two highest chiral orders, I can conclude that predictions are converged and further chiral orders would rather not bring large contribution to the cross section values. The difference

with experimental data is rather systematic and is independent on the chiral order. The relative difference between experimental data and predictions obtained with N^4LO+ and $\Lambda = 450$ MeV at 30 MeV is less than 13 % and absolute difference is $< 3.07 \frac{\mu\text{b}}{\text{sr}}$. At 100 MeV discrepancy is larger and relative difference reaches 46% with absolute difference up to $1.39 \frac{\mu\text{b}}{\text{sr}}$. Coming to 140 MeV the relative difference increases up to 48.6 % and absolute - $1.93 \frac{\mu\text{b}}{\text{sr}}$. What may be helpful for a better data description is a 2N current and relativistic correction, mentioned earlier.

Predictions obtained with Argonne V18 (AV18) potential (dashed-dotted purple line on the Fig. 3.4a) show that it is very similar at lower energies (relative difference at 30 MeV is 0.06 % at the point of maximum - 80°) and with increasing energy to 140 MeV it grows to 3.1 %] at same angle. It can be connected with our potential's quality loss, but AV18 can be struggling with high energies as well.

The Fig. 3.5a presents theoretical truncation uncertainties and it once more confirms that for the regarded nuclear reaction chiral order N^4LO+ is able to produce converged predictions: the black band is hardly visible for the $E_\gamma = 30$ MeV (the relative error for N^4LO+ at 80° is only 0.12 %) and is also quite narrow for larger energies (at 140 MeV the error at the same angle is 1.42 %).

Fig. 3.5b presents a cutoff dependency of predictions. The ideal case is when the dependency is so weak that the choice of the parameter Λ would not make large changes. In practice the choice of this parameter can be important as it makes a noticeable difference in predictions.

On the top of Fig. 3.5b (when $E_\gamma = 30$ MeV) the cutoff dependance is so weak, that, in fact, all the lines (for different Λ values) overlap each other and we cannot distinguish them with the naked eye: the relative difference at maximum is 0.08 %. Nevertheless, with increasing photon's energy to 100 MeV and 140 MeV (middle and bottom rows of Fig. 3.5b) the spread becomes larger: the cutoff error is 3.35 % at 100 MeV and 5.56 % at 140 MeV (the same θ_p).

On the Fig. 2.2 we saw that the total cross section for the same energies has the cutoff spread around 4.5 % for 100 MeV and 8 % for 140 MeV. For 30 MeV it is below 1 %.

In Fig. 3.4b I show different components of the best prediction (N^4LO+ , $\Lambda = 450$ MeV) for three values of photon's energy. Prediction with plane-wave component only (without rescattering part) has relatively small deviation from the full predictions, but the difference increases at larger energies. With $E_\gamma = 30$ MeV the relative difference is 10 % ($4.03 \frac{\mu\text{b}}{\text{sr}}$) at $\theta_p = 80^\circ$. Difference at 100 MeV and the same angle is 4 % ($0.21 \frac{\mu\text{b}}{\text{sr}}$) and at 140 MeV it is 7 % ($0.21 \frac{\mu\text{b}}{\text{sr}}$). In contrast, predictions without Siegert component (1NC) have much larger gap with full prediction: the difference is 46.5 % ($13.67 \frac{\mu\text{b}}{\text{sr}}$) at 30 MeV, 78.6 % ($2.88 \frac{\mu\text{b}}{\text{sr}}$) at 100 MeV and 77.8 % ($1.68 \frac{\mu\text{b}}{\text{sr}}$) at 140 MeV. Obviously 2NC contributions are extremely important in this case, the difference connected with 2NC contributions is much higher than theoretical errors or even rescattering contribution.

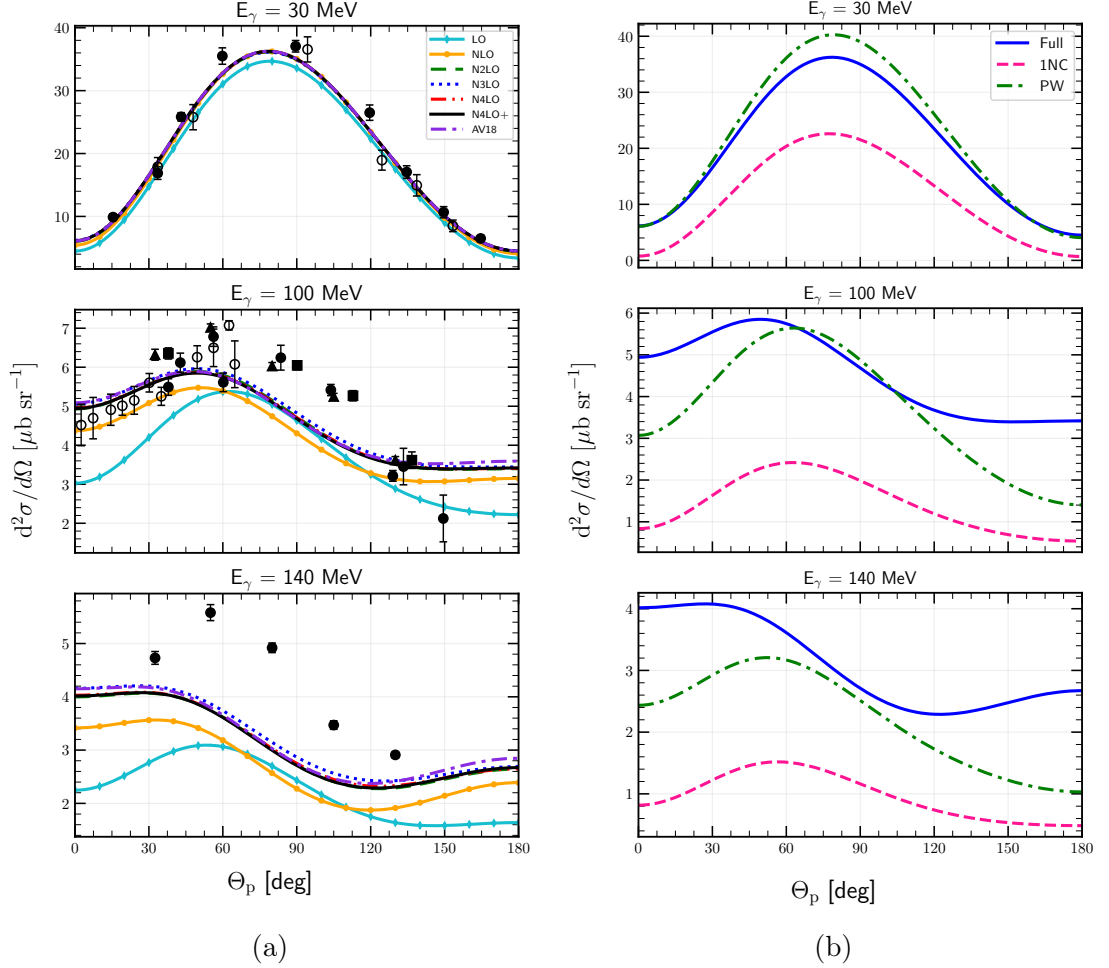


Figure 3.4: Differential cross section as a function of the outgoing proton angle in the center of mass frame for the photon's energy 30 MeV (top), 100 MeV (middle) and 140 MeV (bottom). **(a)** Results obtained using SMS potential at different chiral orders (from LO to $N^4\text{LO}+$) with the cutoff parameter $\Lambda = 450$ MeV and 2NC contributions taking via Siegert theorem. For the sake of comparison, predictions obtained with the AV18 potential are on both figures as well. Data points (filled and empty circles) are from [32] for $E_\gamma = 30$ and 100 MeV and [33] for $E_\gamma = 140$ MeV. **(b)** Predictions obtained with chiral $N^4\text{LO}+$ potential and $\Lambda = 450$ MeV. Blue solid line is a best predictions we have (plane-wave plus rescattering parts, 1NC + Siegert), pink dashed line shows predictions obtained with single-nucleon current only (without Siegert contributions) and green dashed-dotted line is a prediction with plane-wave part only - without rescattering.

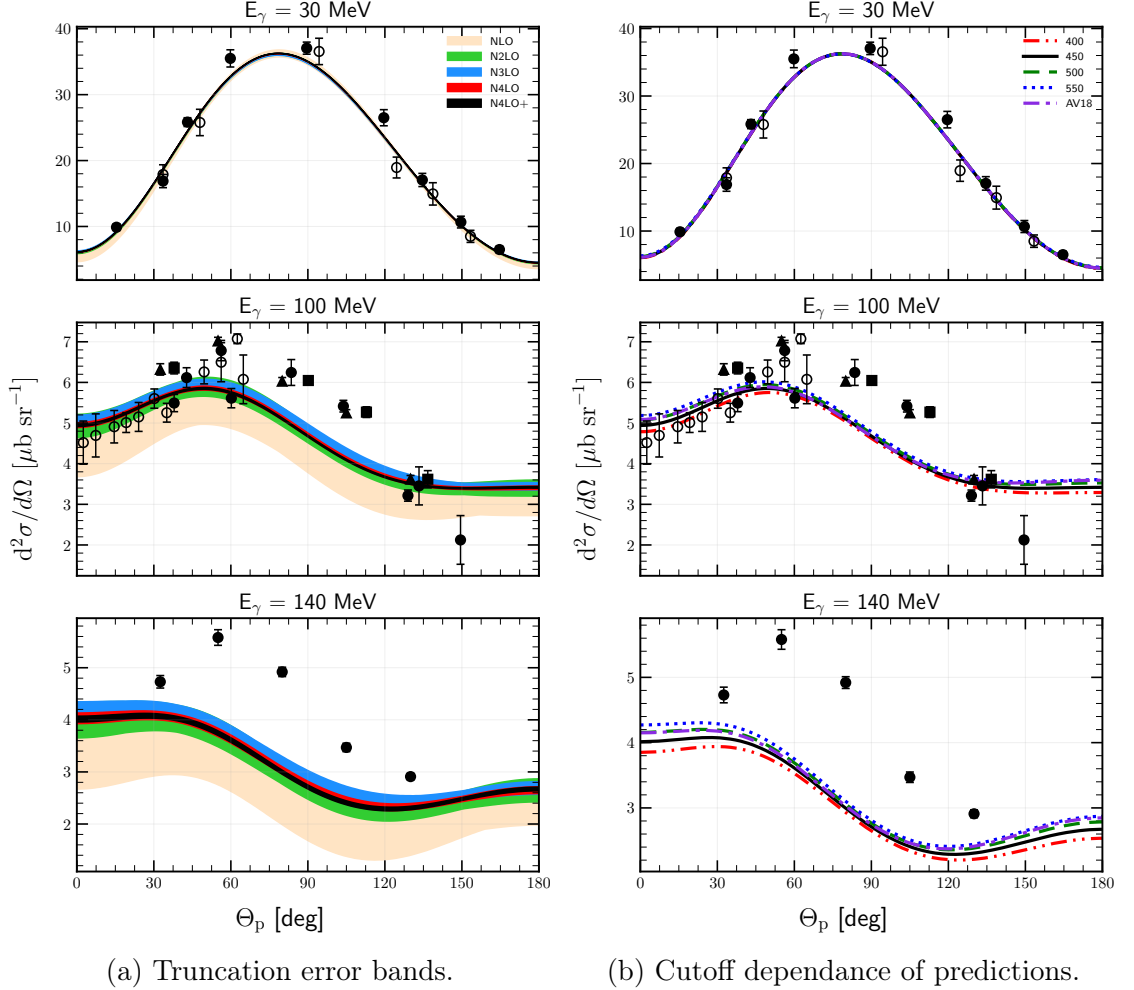


Figure 3.5: Theoretical uncertainties for the differential cross section $\frac{d^2\sigma}{d\Omega}$ as a function of the outgoing proton's momentum polar angle θ_p in the center of mass frame for the photon's energy is 30 MeV (top row), 100 MeV (middle row) and 140 MeV (bottom row). **(a)** The truncation error bands for each energy order in a corresponding row. Results are obtained using potential with different chiral orders (from NLO to N⁴LO+) with cutoff parameter $\Lambda = 450$ MeV and 2NC contributions taking via Siegert approach. **(b)** Predictions obtained using different values of the cutoff parameter Λ (double-dotted-dashed red line presents results obtaining with a cutoff values $\Lambda = 400$ MeV, solid black line - 450 MeV, dashed green line - 500 MeV and dotted blues line - 550 MeV) and the chiral potential N⁴LO+. Data points are the same as in Fig. 3.4a

3.1.2 Polarisation observables

In this subsection I will present my predictions for selected polarisation observables. I start with deuteron analyzing power T_{20} , T_{21} and T_{22} , which according to [6] are defined as:

$$T_{2i}(\theta) = \frac{(2 - \delta_{i0}) \operatorname{Re} V_{2i}}{V_{00}}, i = 0, 1, 2 \quad (3.2)$$

On the Figures 3.6 (a, b) and 3.7(a,b) I show my predictions for the T_{20} , T_{21} , and iT_{11} respectively as a functions of the outgoing proton angle θ in the CM frame. Each of them is prepared with photon's energy 30 MeV and is organized in the similar way: the top pane shows a dependance of the predictions on the chiral order of the potentia. The middle subfigure is showing a correspondent truncation error for each of the predictions from a top one (without LO, because its uncertainty is too large and will make the readability worse). The last (bottom) pane shows the cutoff dependance for each observable at the chiral order $N^4\text{LO}+$.

All the polarisation observables presented here, show a good convergence upon a chiral order as it is hard to distinguish the predictions from each subsequent order starting from the $N^2\text{LO}$. The relative width of $N^4\text{LO}+$ truncation band for T_{20} , T_{21} and T_{22} are 0.06 %, 0.05 % and 0.19 % respectively (at $\theta_p = 90^\circ$, 60° and 90° respectively). The slowest convergence is observed for iT_{11} (Fig. 3.7b) where we can still recognize $N^2\text{LO}$ band. Still it has only a 0.2 % width of $N^4\text{LO}+$ truncation band at $\theta_p = 20^\circ$ (maximum point). The cutoff dependency for all regarded observables is weak and predictions for each value of the Λ are hardly separable with the naked eye. The relative spread of cutoff predictions at the same angles as above are 0.87 %, 0.94 %, 3.42 % and 0.68 % respectively for T_{20} , T_{21} , T_{22} and iT_{11} respectively.

Predictions for the photon's energy $E_\gamma = 100$ MeV (Figs. 3.8 and 3.9) preserve similar trends for each obserable. Generally, predictions are being converged starting even from the $N^2\text{LO}$ while for iT_{11} we can see that truncation error's bands are noticeably wide even at $N^4\text{LO}$ and $N^4\text{LO}+$ Cutoff dependance at this energy is a bit stronger, especially for T_{22} and iT_{11} components (Fig. 3.7), where one can see slightly stronger discrepancy at the stationary points.

Looking at the predictions for the deuteron tensor analyzing power, we can conclude that cutoff dependence is generally weak and the choice of Λ does not affect predictions much: the relative spread among all cutoffs for T_{20} is 2.28 % around the point of maximum ($\theta_p = 90^\circ$). For other components of the tensor analyzing power spread is: T_{21} - 0.5 % at $\theta_p = 60^\circ$; T_{22} - 4.1 % at $\theta_p = 90^\circ$; iT_{11} - 11.4 % at $\theta_p = 20^\circ$. We see that iT_{11} has much larger spread in the maximum point and is more sensitive to the cutoff choice.

In the case of the chiral order convergence, we can also see that predictions are mostly converged after $N^2\text{LO}$ or $N^3\text{LO}$. The relative width of $N^4\text{LO}+$ truncation band for T_{20} , T_{21} and T_{22} are 0.7 %, 0.7 % and 0.04 % respectively (at the same angles as the spread was shown above). One exception here is also a iT_{11} for which this width is much larger - 6.8 % at $\theta_p = 20^\circ$. The truncation uncertainty is much lower then one, connected to the choice of cutoff parameter. iT_{11} seem to be more sensitive both to the choice of cutoff parameter and to the chiral order. Even for this observable cutoff spread is almost twice larger than truncation error's band. Standing out of other tensor components, iT_{11} can be usefull for the investigation of global convergence with respect to the chiral order and cutoff dependance of the model. Of course, we can also confirm once more that our model is less accurate at higher energies which is reflected in a stronger cutoff dependance and

slower chiral convergence.

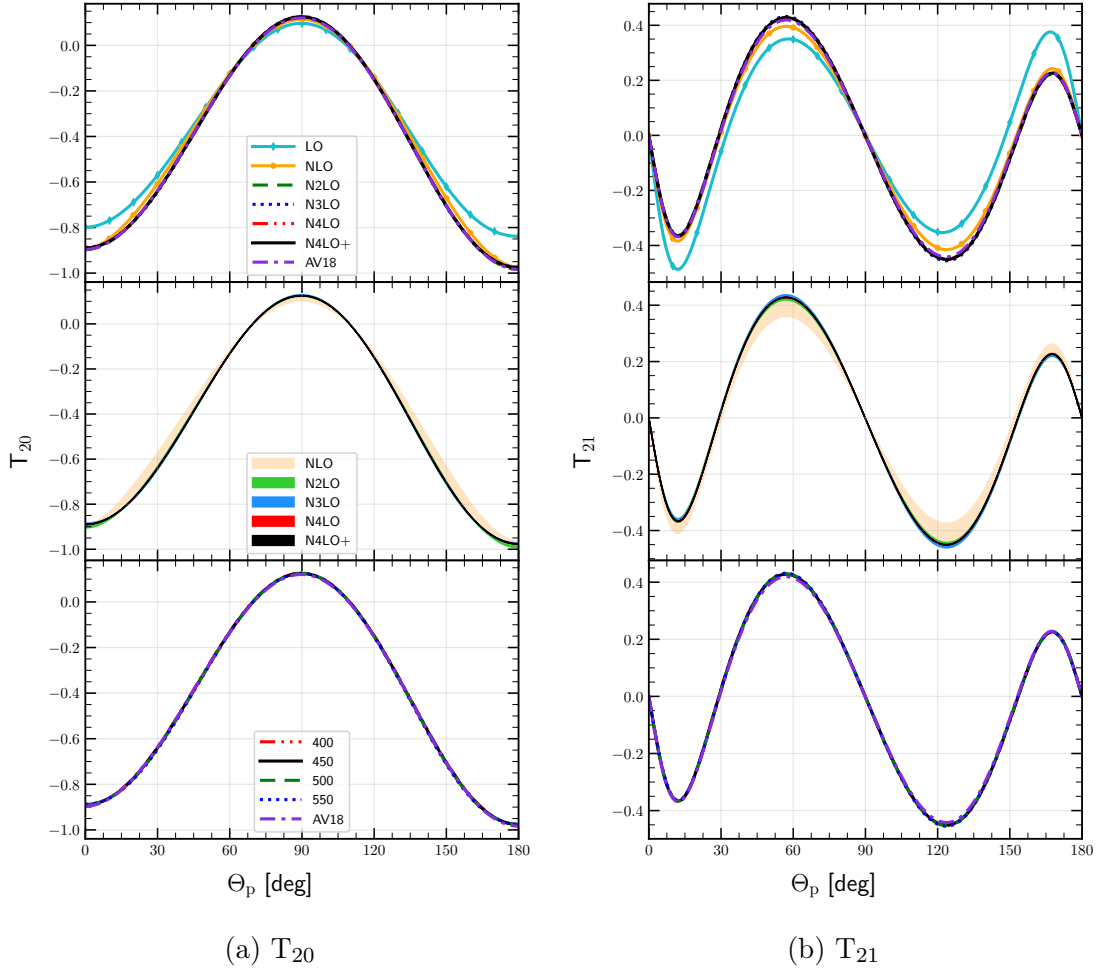


Figure 3.6: Tensor analyzing power T_{20} (a) and T_{21} (b) as a function of the outgoing proton angle in the center of mass frame for the photon's energy 30 MeV. Top row presents results obtained using potential with different chiral orders (from LO to $N^4\text{LO}+$) with cutoff parameter $\Lambda = 450$ MeV. The middle row shows truncation errors for each chiral order starting from NLO and bottom row presents a cutoff dependency (chiral potential $N^4\text{LO}+$). For the sake of comparison, predictions obtained with AV18 potential are on figures as well.

In Fig. 3.10 together with best prediction at $E_\gamma = 30$ MeV ($N^4\text{LO}+$, $\Lambda = 450$ MeV, Siegert theorem), I show predictions obtained with 1NC only and with plane-wave contribution without rescattering part. In case of deuteron's tensor analyzing power components, the contribution of rescattering part is not that big for T_{20} , T_{21} and T_{22} (up to 20 % in extremum points). Nevertheless, for iT_{11} we see that PW part equals to zero. It may be connected with some features of this particular components, such that plane-wave part cancels out. The 2NC component taken into account via Siegert theorem has a dominant contribution here. We see that 1NC predictions are absolutely away from the Full predictions and in case of iT_{11} does not even reflect total prediction qualitatively.

Fig. 3.11 presents similar results but for $E_\gamma = 30$ MeV and it is interesting that difference between Full and 1NC prediction becomes smaller and it is especially visible for T_{22} . At this energy the relative difference at $\theta_p = 90^\circ$ is 43.6 % comparing to 122.8 % at $E_\gamma = 30$ MeV. Similarly, the difference for T_{20} at $E_\gamma = 30$ MeV ($\theta_p = 90^\circ$) is 91.4 % and

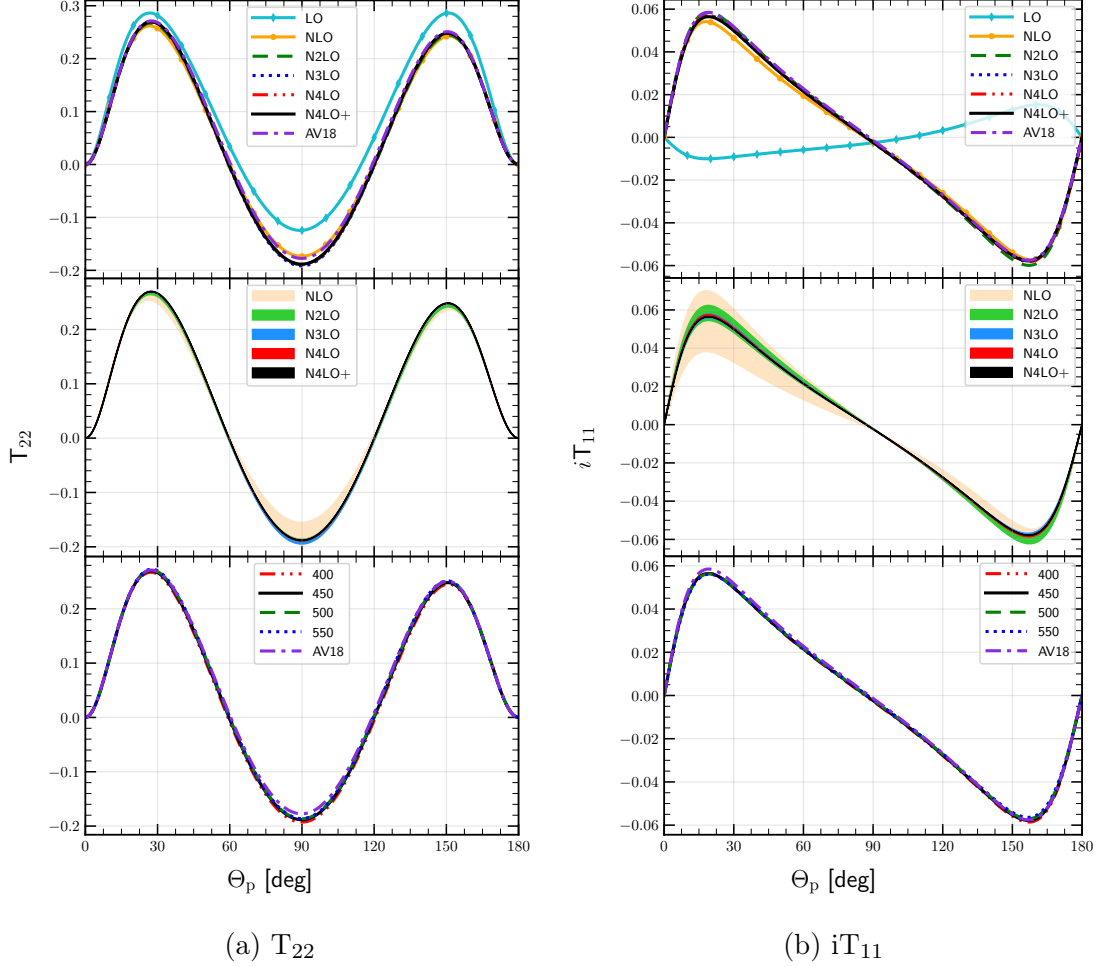


Figure 3.7: The same as on 3.6 but for polarisation observables T_{22} (subfigure (a)) and iT_{11} (subfigure (b)).

at $E_\gamma = 100$ MeV it drops down to 28.8%. This trend is noticeable looking on Figures (3.12 - 3.18). With

On the next figures, I show the predictions in a similar way as it was done in [31] in order to compare my predictions with the experimental data. On the Figures 3.12 - 3.18 I show an angular dependance of the T_{2i} ($i = 0, 1, 2$) for a specific energy bands. Solid blue line shows an average value of the observable in the specified energy range obtained at N⁴LO+ with $\Lambda = 450$ MeV, while the pink dashed line is a prediction obtained with a same setup but without using a contributions from Siegert approach (single nucleon current only). Bands for each of prediction specify the spread of predictions in regarded energy band.

One can see that the data description is better for the predictions with Siegert contributions and SN current is not able to describe experiment properly. With increasing energy (more than 100 MeV), the difference between predicted values and experimental data becomes larger (especially for T_{22}), but the model I use is not meant to be used for high energies and figures are presented out of the curiosity.

On the Figure 3.19 the energy dependance of T_{20} and T_{22} (integrated over all angles) is presented for the energy range 0-400 MeV. I also demonstrate the experimental data from [31] and [34] as well as theoretical calculations from [35] on the figure. For T_{20} the model is able to describe experimental data well even for high energies. On the

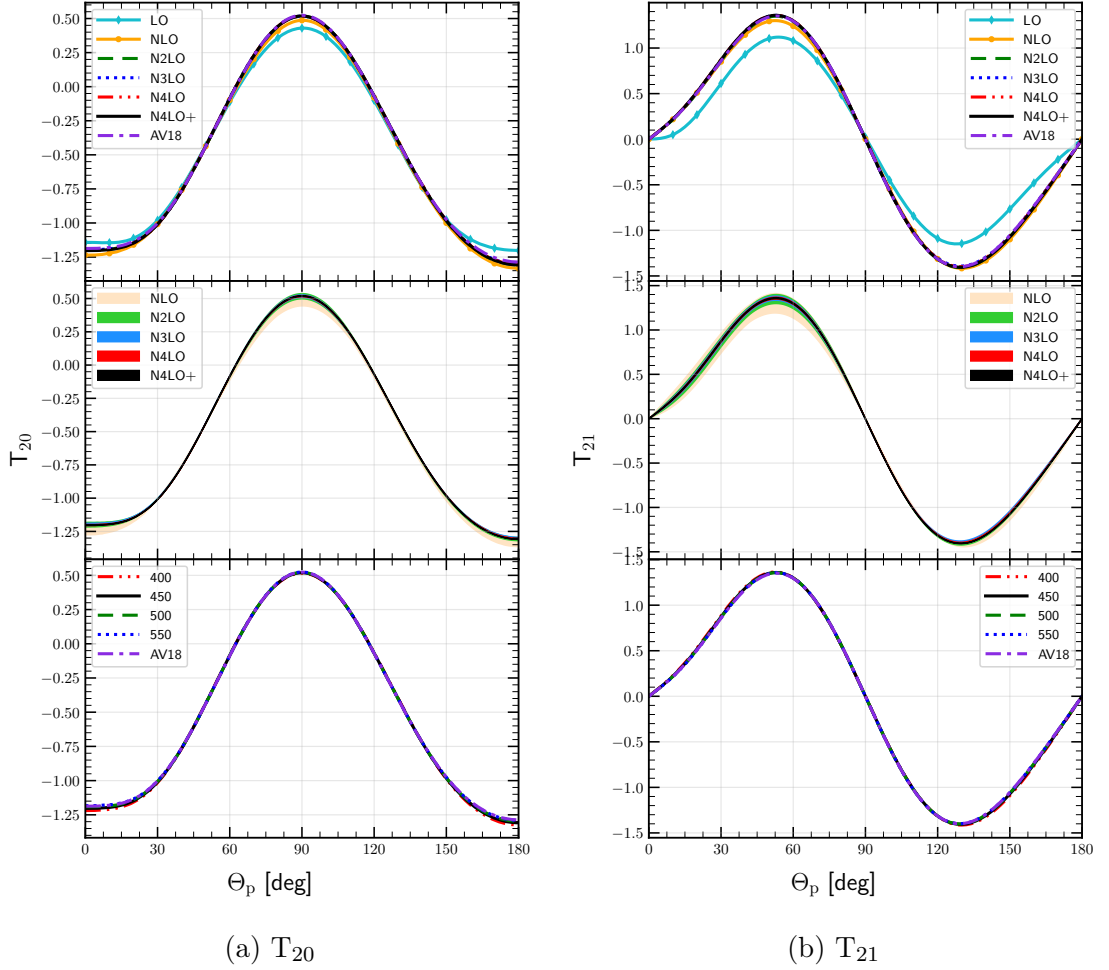


Figure 3.8: Tensor analyzing power T_{20} **(a)** and T_{21} **(b)** as a function of the outgoing proton angle in the center of mass frame for the photon's energy 100 MeV. Top row presents results obtained using potential with different chiral orders (from LO to N⁴LO+) with cutoff parameter $\Lambda = 450$ MeV. The middle row shows truncation errors for each chiral order starting from NLO and bottom row presents a cutoff dependency (chiral potential N⁴LO+). For the sake of comparison, predictions obtained with AV18 potential are on figures as well.

other hand, T_{22} is not so well described: for the low energies the prediction curve is somehow within uncertainties of experimental data, but further the difference with the data becomes larger. Also it is not reflect the qualitative nature of the data as we can see that after around 150 MeV data points start ascending which is not represented in my predictions. Theoretical predictions from [35] (brown dashed curve) are also not able to describe data quantitatively for T_{22} , but the growth is presented there.

Similar situation is on the Figures 3.20 and 3.21 where I show an energy dependance of Deuteron analyzing power components for specific angular ranges (following the data from [31]). Predictions for T_{20} are able to reflect the experimental results, while for T_{21} and T_{22} predictions are reasonable (quantitative-wise) only for lower energies and difference with data becomes larger when energy increases. Predictions for T_{22} once more confirm an insufficiency of SN and an importance of 2-nucleon current contributions.

On the Fig. 3.22 I demonstrate predictions for the photon asymmetry Σ_γ for the deuteron photodisintegration with $E_\gamma = 20$ MeV (a) and 60 MeV(b) as well as experimental

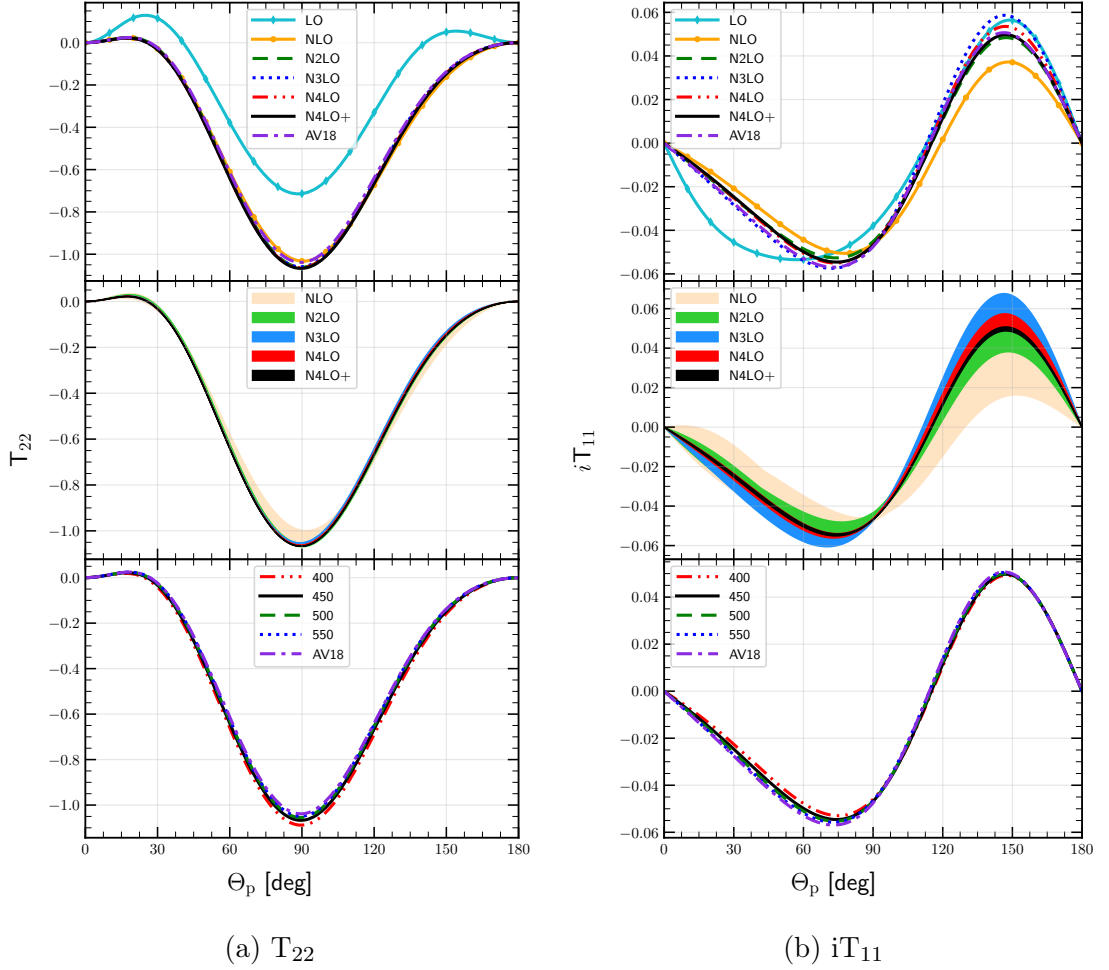


Figure 3.9: The same as on 3.8 but for polarisation observables T_{22} (subfigure (a)) and iT_{11} (subfigure (b)).

data. Both (a) and (b) figures are organized similarly to the figures I showed earlier for the tensor analyzing power (e.g. Fig. 3.7). That is the top pane is aimed to demonstrate predictions obtained with chiral potential at different orders, the middle one is showing a truncation error bands and the bottom - shows the cutoff dependance. What we can see here is good convergence with respect to the chiral order. For both regarded energies predictions at different orders are very close to each other except for LO and NLO curves. Nevertheless, at 60 MeV we can see that truncation error bands reveal some uncertainty connected with the chiral order and I can assume that even some higher chiral orders would still contribute to the predictions at this energy.

Cutoff dependance is also stronger at 60 MeV. We can clearly see that predictions are different for each value of the Λ . The standard deviation with respect to the cutoff parameter at 20 MeV does not exceed 0.7% of the mean value while at the photon's energy 60 MeV the maximum value is around 2.5% (at $\theta = 115^\circ$).

Regarding the correspondance to experimental data, we can clearly see that for the lower energy predictions are almost perfectly overlapping with experimental point (and error bars). Few points are laying outside the predictions but it can be caused by experimental issues. For 60 MeV, experimental data points are constantly below prediction curves (especially in the middle of angles range). It seems that some systematic uncertainty is presented in predictions and multiplication by some factor (presumably less than 1)

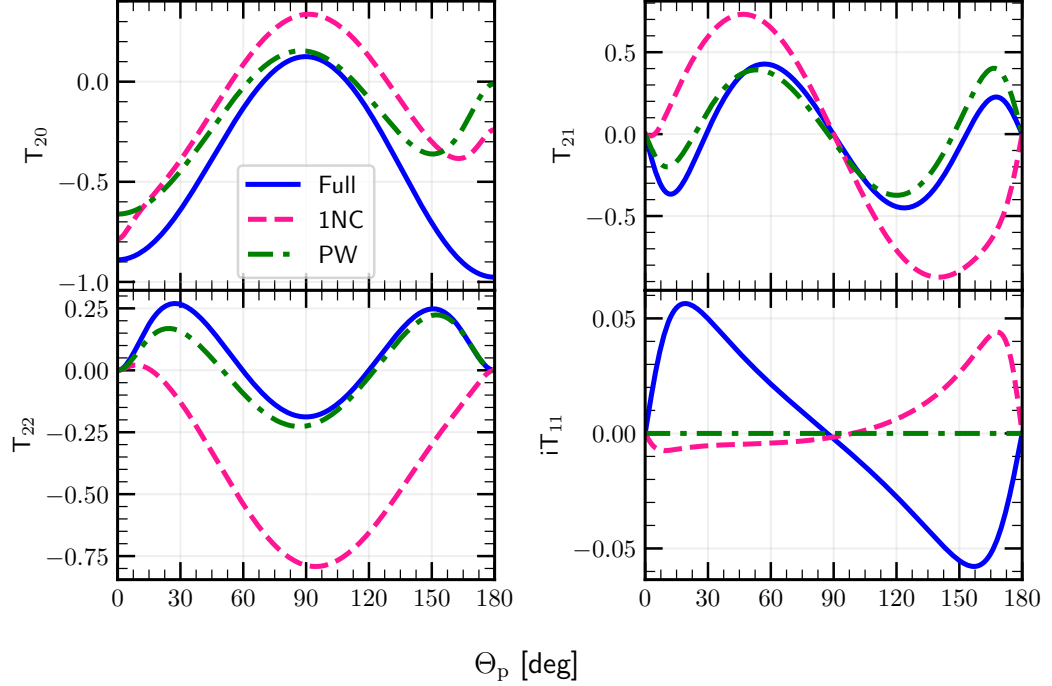


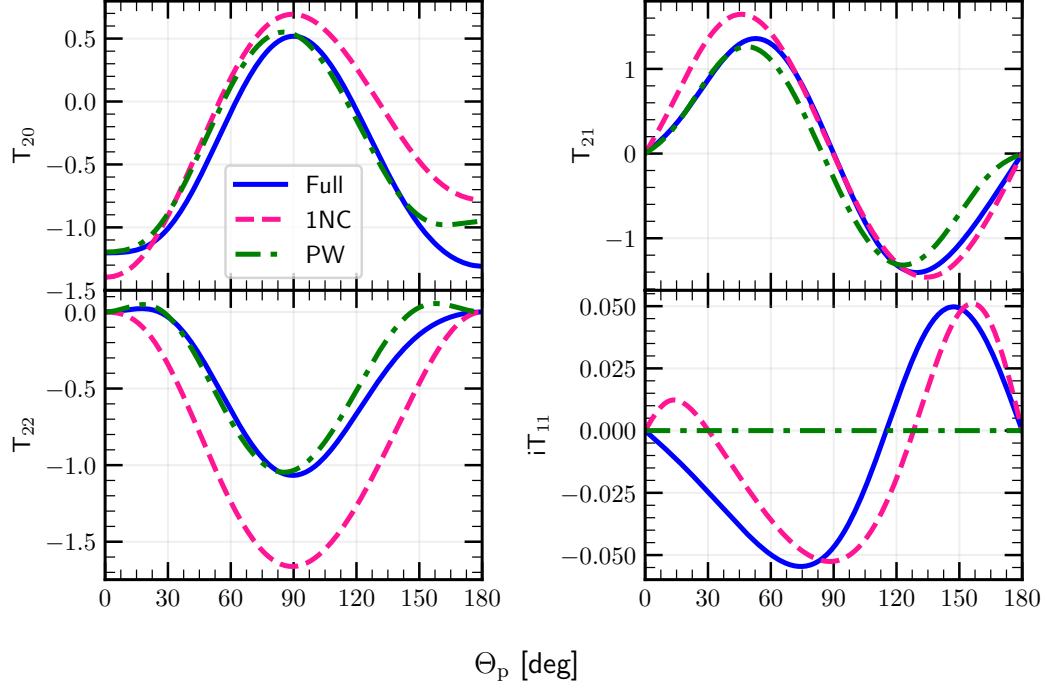
Figure 3.10: Tensor analyzing power components T_{20} , T_{21} , T_{22} and iT_{11} as a functions of the outgoing proton angle θ_p (in the center of mass frame) at $E_\gamma = 30$ MeV. Similarly to Fig. 3.4b predictions obtained with chiral $N^4\text{LO}+$ potential and $\Lambda = 450$ MeV are presented for each component. Blue solid line is a best predictions we have (plane-wave plus rescattering parts, 1NC + Siegert), pink dashed line shows predictions obtained with single-nucleon current only (without Siegert contributions) and green dashed-dotted line is a prediction with plane-wave part only - without rescattering.

could help predictions be more similar to experimental data.

On the Fig. 3.23 I present dependance of the asymmetry Σ_γ on the photon's energy with fixed value of the outgoing proton's angle $\theta_p = 90^\circ$ (following the data given at [36] and [37]). It is noticeable that with increasing energy, the prediction curve becomes more and more above the experimental data. This trend was also observed in angular dependance of the asymmetry at 60 MeV so I can assume that within our framework, Σ_γ is sensitive to the initial photon's energy and some contributions are missing in order to prepare good predictions at higher energies. From the Fig. 3.23 we can say that large discrepancy with data starts appearing after 35 MeV.

The proton polarization is demonstrated on the Fig. 3.24 for the photon's energy 30 MeV(a) and 100 MeV(b). In this case even higher energy such as 100 MeV does not reveal neither slower convergence with respect to the chiral order no stronger cutoff dependence. Figures for both energies show that only next-to-leading order brings relatively high contribution while taking into account each subsequent order does not change predictions largely. In the case of cutoff dependance, we see that curves for each value of Λ are very close to each other. The standard deviation of the predictions with respect to the cutoff parameter has maximal value 1.94% at $E_\gamma = 30$ MeV and 3.2% at 100 MeV. The dependance is slightly stronger for higher energy, but these values are comparable.

Predictions for the neutron polarization at energy 2.75 MeV and 100 MeV are on the Fig. 3.25. The choice of energy is conditioned by the availability of experimental data.


 Figure 3.11: The same as on Fig. 3.10 but for $E_\gamma = 100$ MeV

In case of $E_\gamma = 2.75$ MeV (Fig. 3.25a), we can see that predictions reflect the behavior of experimental data points qualitatively, having more or less constant offset of the values. Similar offset was obtained also in predictions at [6], where various approaches were presented. Interesting is that predictions clearly show symmetrical form of the curve, while in the experimental data have some deviations from symmetrical form. It can be a sign that some problem with data can be in this case (taking into account also that experiment had been done in 196) as well as inaccuracy in theoretical models.

At the energy $E_\gamma = 100$ MeV (Fig. 3.25b), the difference with experimental data does not look like a systematic shift and deviations look like random. For most of data points, predicted values are within error bars and only some of points (e.g. around 50°) have prediction completely out of measured data. Nevertheless, these data points look like being out of general trend and may be a result of unprecise measurement.

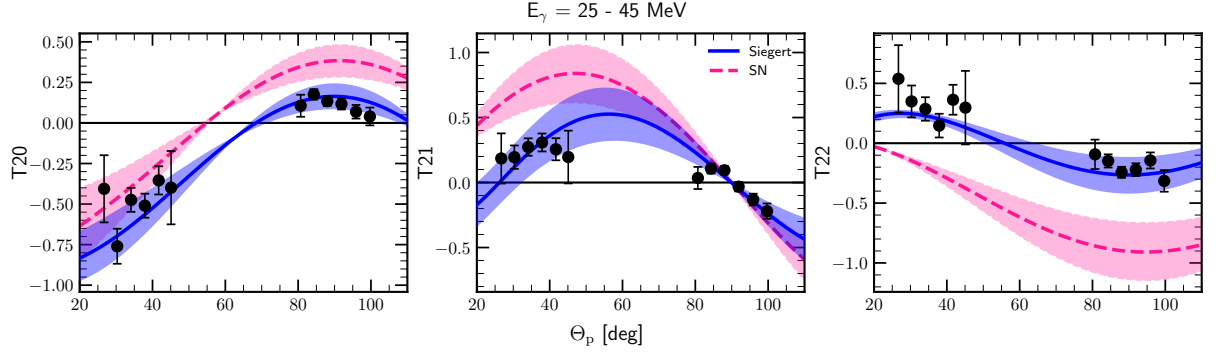


Figure 3.12: Tensor analyzing powers T_{20} , T_{21} and T_{22} as a functions of the outgoing proton angle θ_p (in the center of mass frame). Solid blue line is a mean value of my predictions obtained with a SMS potential at N⁴LO+ chiral order and with $\Lambda = 450$ MeV at energy values from 25 to 45 MeV and where SN current was used together with Siegert approach. Pink dashed line is similar prediction but with SN only. The corresponding bands show the deviation of predictions in the regarded energy region. Filled circles are experimental data from [31] for the analogous energy span.

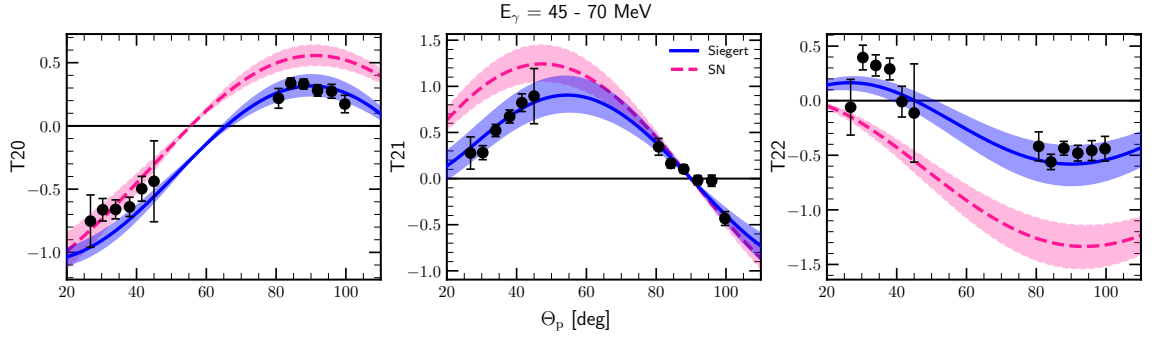


Figure 3.13: The same as on the Fig. 3.12 but for energy bin 45 – 70 MeV

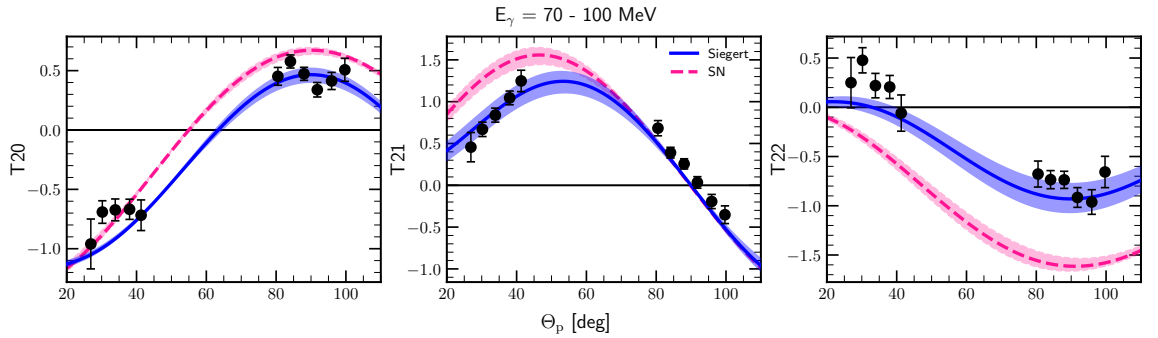


Figure 3.14: The same as on the Fig. 3.12 but for energy bin 70 – 100 MeV

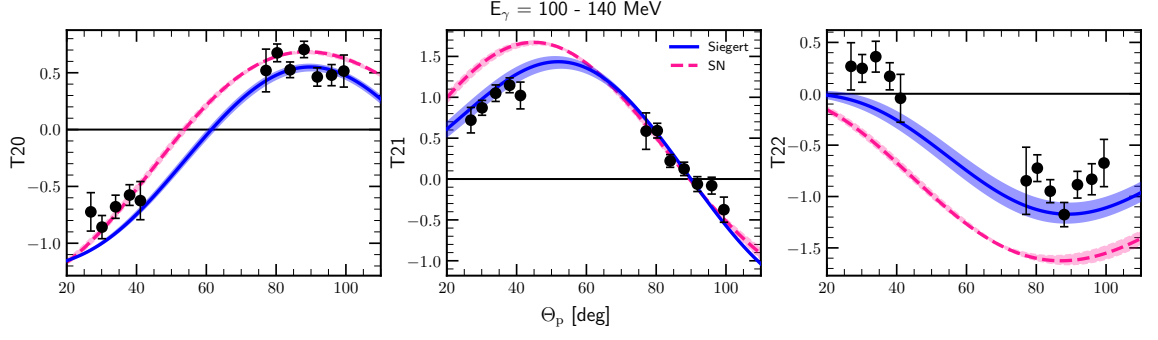


Figure 3.15: The same as on the Fig. 3.12 but for energy bin 100 – 140 MeV

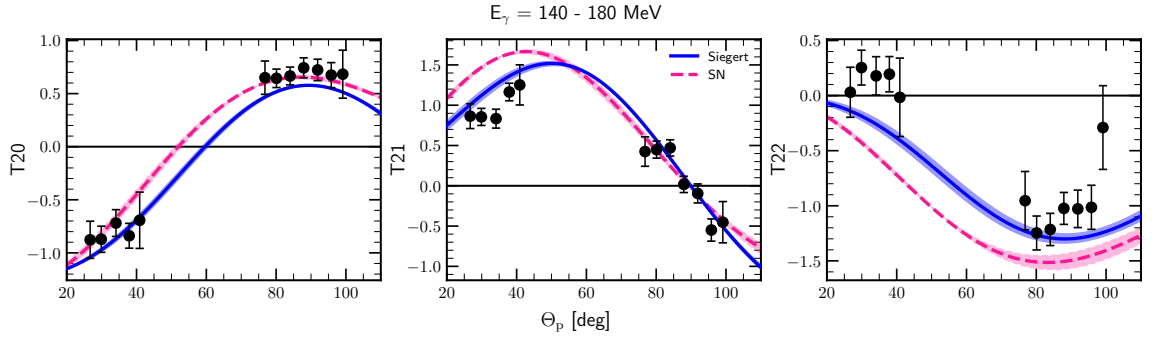


Figure 3.16: The same as on the Fig. 3.12 but for energy bin 140 – 180 MeV

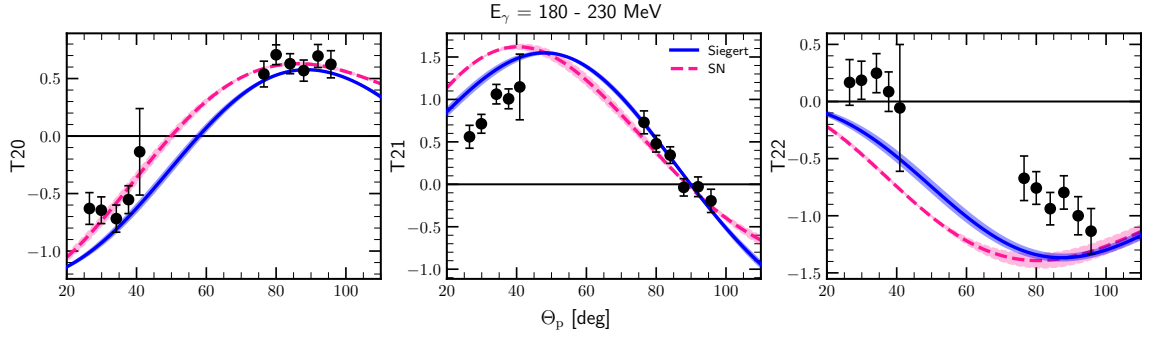


Figure 3.17: The same as on the Fig. 3.12 but for energy bin 180 – 230 MeV

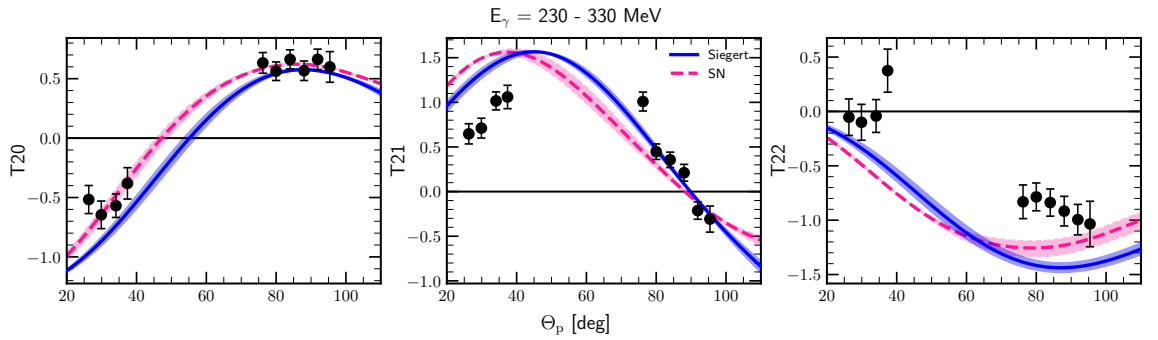


Figure 3.18: The same as on the Fig. 3.12 but for energy bin 230 – 330 MeV

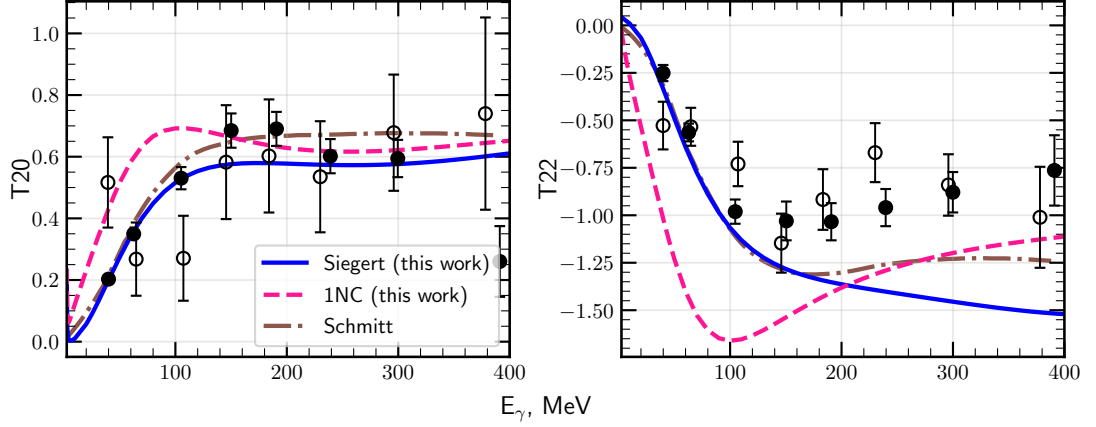


Figure 3.19: Tensor analyzing powers T_{20} and T_{22} as a functions of the photon energy E_γ with fixed outgoing proton angle $\theta_p = 88^\circ$ (in the center of mass frame). My predictions (blue solid line) are obtained with SMS potential at chiral order $N^4\text{LO}+$ and with cutoff parameter $\Lambda = 450 \text{ MeV}$ with 2NC contributions included via Siegert theorem, dashed pink line show prediction obtained without 2NC contributions. Dashed-dotted brown line presents calculations from [35]. Experimental data is taken from [31] (filled circles) and [34] (empty circles).

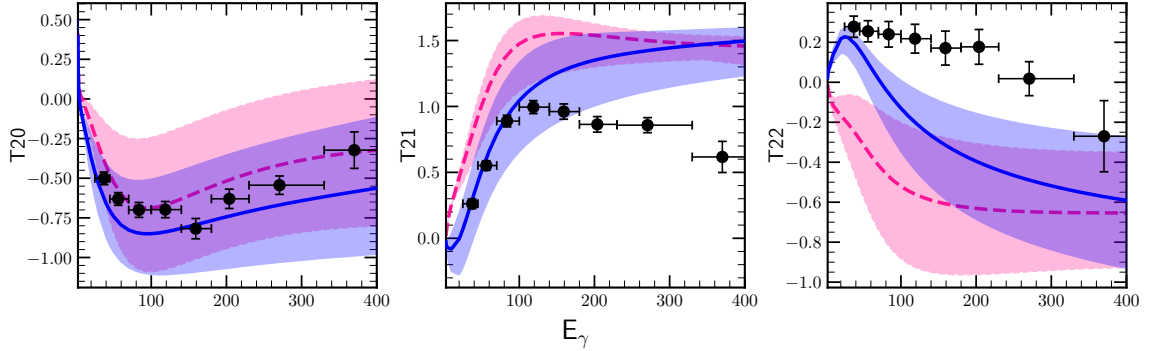


Figure 3.20: Tensor analyzing powers T_{20} , T_{21} and T_{22} as a functions of the photon's energy within the outgoing proton's angle range $24^\circ - 48^\circ$ (in the center of mass frame). Solid blue line is a mean value of my predictions obtained with SMS potential at $N^4\text{LO}+$ chiral order and with $\Lambda = 450 \text{ MeV}$ at energy values from 25 to 45 MeV within a given angles range and where SN current was used together with Siegert approach. Pink dashed line is similar prediction but with SN only. The corresponding bands show the deviation of predictions in the regarded energy region. Filled circles are experimental data from [31] for the analogous energy span.

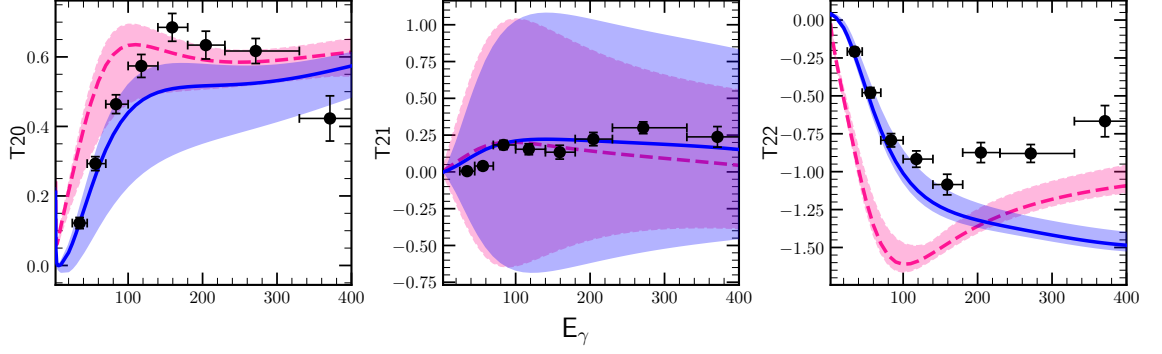
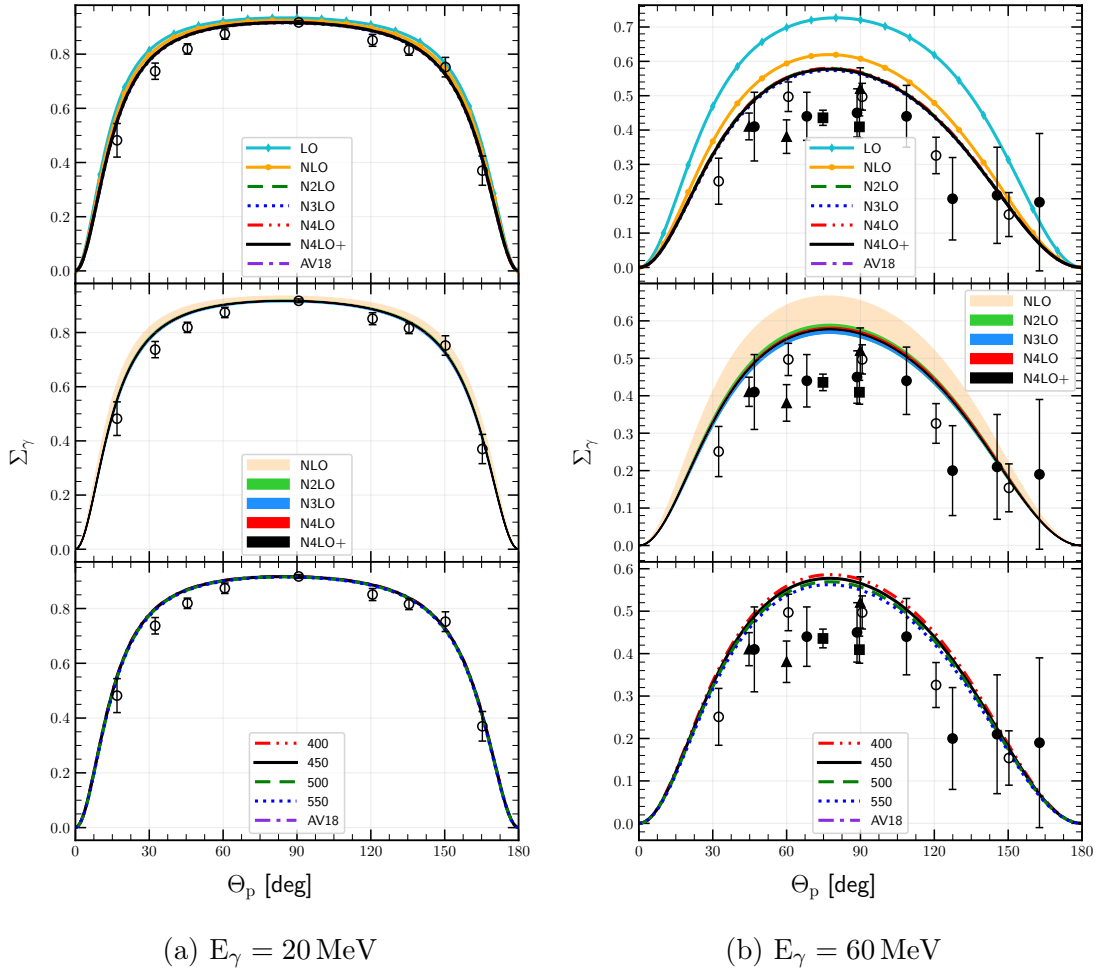

 Figure 3.21: The same as on the Fig. 3.20 but for the angles' range $70^\circ - 102^\circ$.


Figure 3.22: The photon asymmetry Σ_γ as a function of the outgoing proton angle in the center of mass frame for the photon's energy 30 MeV(a) and 100 MeV(b). Top row presents results obtained using potential with different chiral orders (from LO to $N^4\text{LO}+$) with cutoff parameter $\Lambda = 450 \text{ MeV}$. The middle row shows truncation errors for each chiral order starting from NLO and bottom presents a cutoff dependency (chiral potential $N^4\text{LO}+$). Filled circles are experimental data from [38], empty circles - from [37], filled squares - from [39] and triangles are from [40]. For the sake of comparison, predictions obtained with AV18 potential are on figures as well.

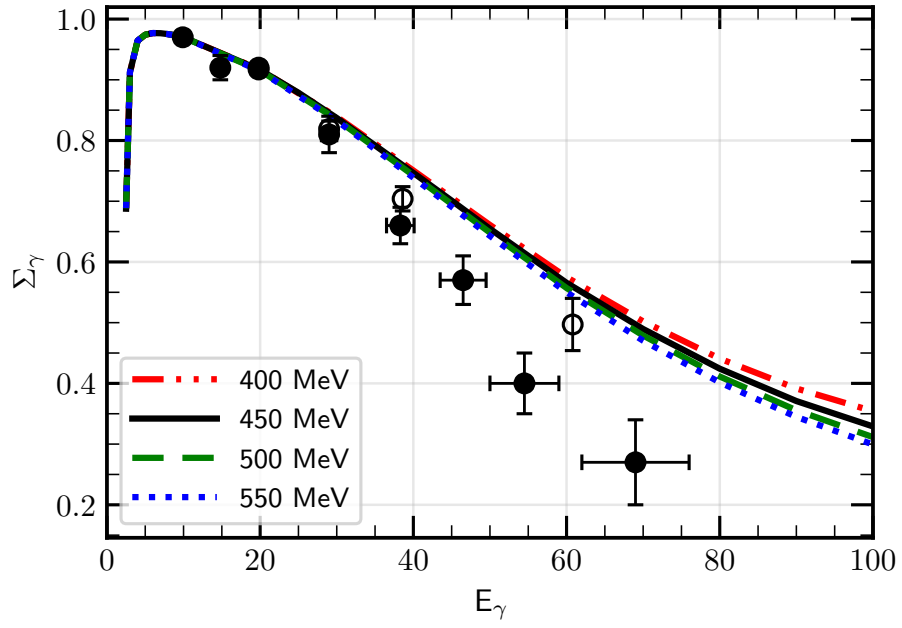


Figure 3.23: The photon asymmetry Σ_γ as a function of the photon energy with fixed outgoing proton angle $\theta_p = 90^\circ$. Each curve corresponds to the particular value of the cutoff parameter and chiral potential used here is $N^4\text{LO}+$. Filled circles are experimental data from [36], empty circles - from [37].

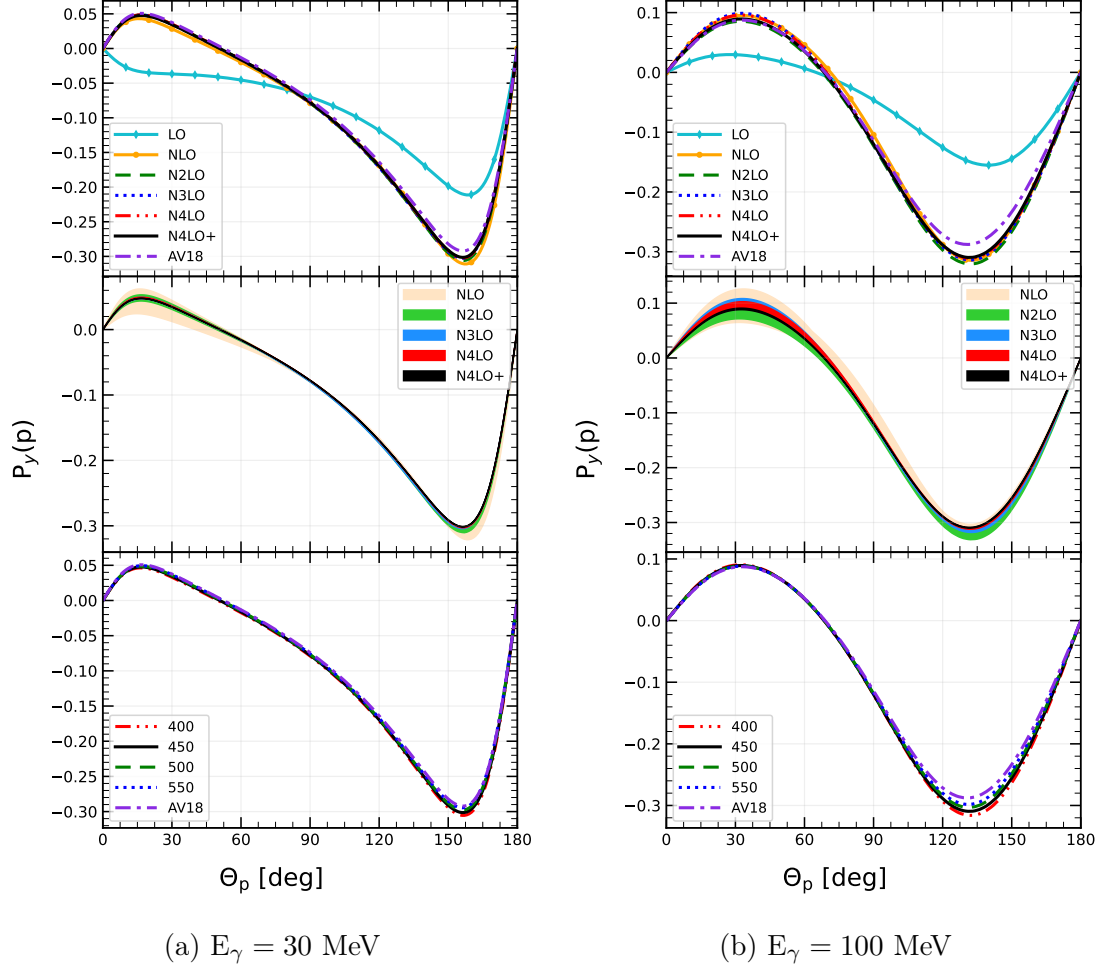


Figure 3.24: Proton polarisation $P_y(p)$ as a function of the outgoing proton angle in the center of mass frame for the photon's energy 30 MeV (a) and 100 MeV (b). Top figure presents results obtained using potential with different chiral orders (from LO to N⁴LO+) with cutoff parameter $\Lambda = 450$ MeV. The middle pane shows truncation errors for each chiral order starting from NLO and bottom figure presents a cutoff dependency (chiral potential N⁴LO+). For the sake of comparison, predictions obtained with AV18 potential are on figures as well.

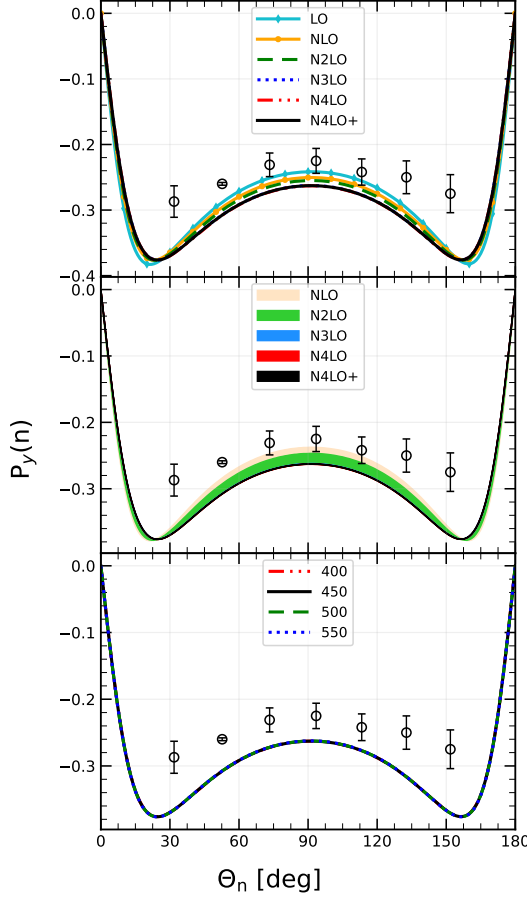
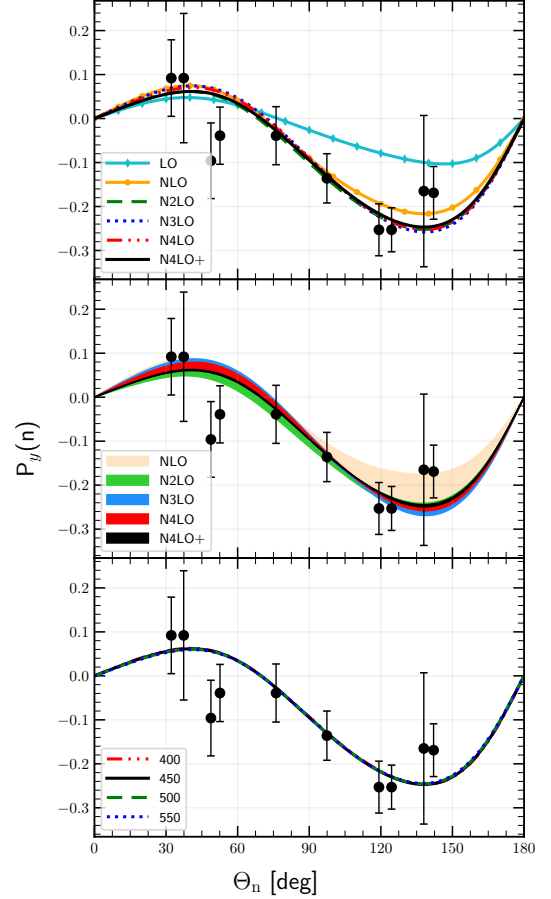

 (a) $E_\gamma = 2.75$ MeV

 (b) $E_\gamma = 100$ MeV

Figure 3.25: Neutron polarisation $P_y(n)$ as a function of the outgoing neutron angle in the center of mass frame for the photon's energy 2.75 MeV(a) and 100 MeV(b). Top row presents results obtained using potential with different chiral orders (from LO to $N^4\text{LO}+$) with cutoff parameter $\Lambda = 450$ MeV. The middle pane shows truncation errors for each chiral order starting from NLO and bottom figure presents a cutoff dependency (chiral potential $N^4\text{LO}+$). Experimental data is from [41] (empty circles) and [42] (filled circles).

3.2 Helium photodisintegration

3.2.1 3N photodisintegration

In this section I will demonstrate predictions for observables from ${}^3\text{He} \rightarrow p + p + n$ process.

On the Fig. 3.26 I demonstrate a differential cross section $\frac{d^5\sigma}{d\Omega_1 d\Omega_2}$ as a function of the S curve position. The photon's energy is $E_\gamma = 30$ MeV and the kinematic configuration $\theta_1 = 15^\circ$, $\phi_1 = 0^\circ$, $\theta_2 = 15^\circ$, $\phi_2 = 180^\circ$; predictions have been obtained without 3NF. We see that only NLO and N²LO introduce relatively large truncation error. The maximal width of a band for NLO is 37.6 % at $S = 10$ MeV, for N²LO it is 12.4 % at the same point and it is gradually decreasing coming to 0.13 % at N⁴LO+. The cutoff spread around maxima values is less than 3 % and it is 0.78 % at the minimum point ($S = 10$ MeV).

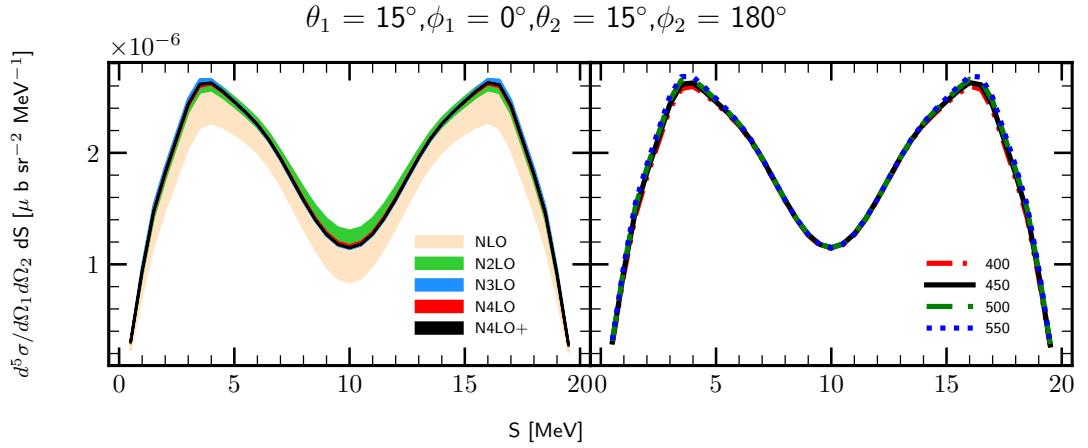


Figure 3.26: The five-fold differential cross section for the photon energy $E_\gamma = 30$ MeV for the kinematic configuration $\theta_1 = 15^\circ$, $\phi_1 = 0^\circ$, $\theta_2 = 15^\circ$, $\phi_2 = 180^\circ$. The left figure presents truncation error bands obtained using potential with different chiral orders (from NLO to N⁴LO+) with cutoff parameter $\Lambda = 450$ MeV. The right figure presents a cutoff dependency (chiral potential N⁴LO+). Results are obtained with two-nucleon force only.

With larger energy $E_\gamma = 100$ MeV demonstrated on the Fig. 3.27, both truncation error and cutoff spread become larger. The truncation band at the maximum point $S = 10$ MeV for NLO is 55.0 % decreasing to 2.2 % at N⁴LO+ which is around 3 times larger than it was in predictions with $E_\gamma = 30$ MeV. The cutoff spread also becomes larger with increasing energy value: 9.0 % at the same (maximum) point which is also ~ 3 times larger than the one we observed for lower energy.

Next I come to other angular configurations for $E_\gamma = 100$ MeV, starting with $\theta_1 = 75^\circ$, $\phi_1 = 75^\circ$, $\theta_2 = 75^\circ$, $\phi_2 = 105^\circ$ demonstrated on Fig. 3.28. Similar predictions but with 3NF contribution is presented on Fig. 3.29. It seems that 3NF does not change much the convergence with respect to the chiral order: truncation error band at the point of maximum $S = 35$ MeV (N⁴LO+) is 1.11 % and 1.16 % with and without 3NF respectively. So it is almost the same, meaning that 3NF contribution does not affect chiral order convergence much.

The cutoff dependence, in turn, is affected by 3NF presence. Predictions with 2NF only have 13.7 % spread at the same maximum point, while predictions with 3NF have 1.23 %, so the difference is tremendous.

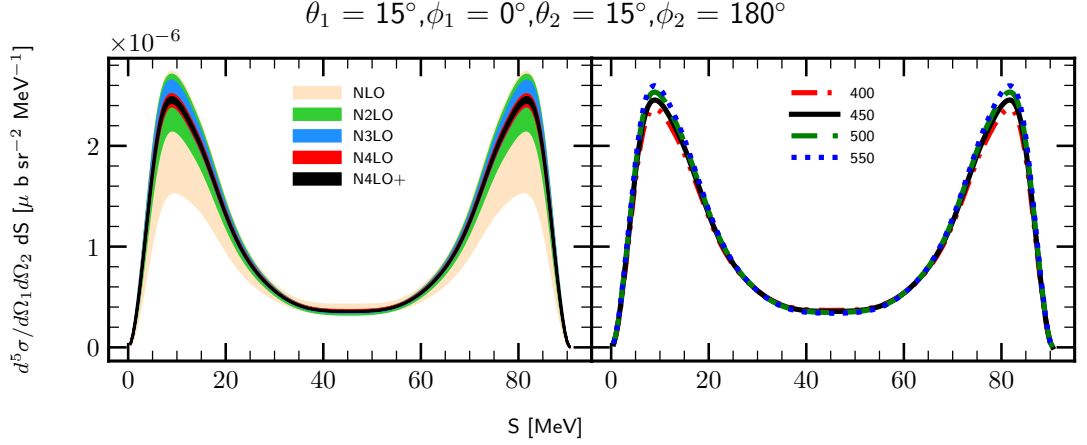


Figure 3.27: The same as on Fig. 3.26 but for the photon energy $E_\gamma = 100$ MeV

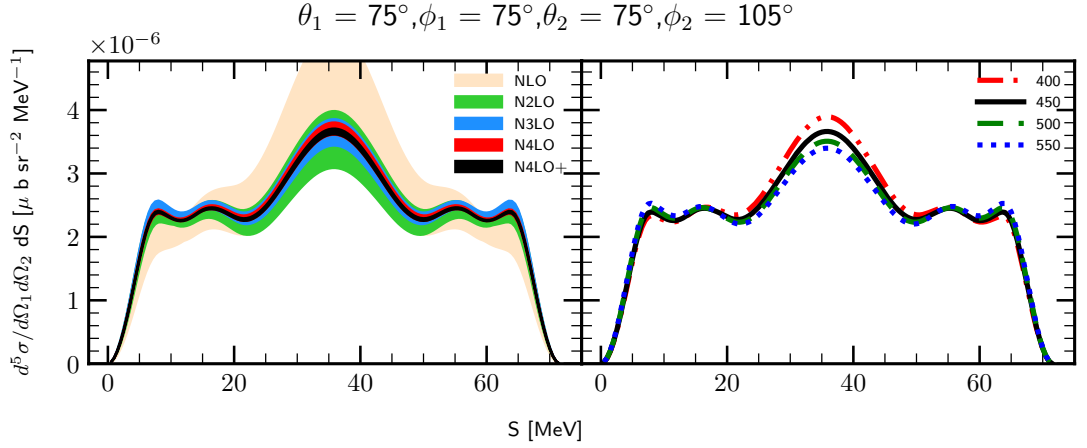


Figure 3.28: The same as on the Fig. 3.27 but for the different kinematic configuration.

Similar trends present in other configurations, demonstrated for the comparison: Figs.3.30 and 3.31, Figs.3.32 and 3.33, Figs.3.34 and 3.35.

The semi-inclusive differential cross section $\frac{d^3\sigma}{d\Omega_p dE_p}$ as a function of the outgoing protons energy E_p is demonstrated on the Fig. 3.36 (for $E_\gamma = 30$ MeV) and Fig. 3.37 (for $E_\gamma = 100$ MeV). Each figure consists of subfigures where each row presents results for a proton angles $\theta_p = 10^\circ, 50^\circ, 90^\circ, 130^\circ$ and 170° . The left part of each subfigure shows a chiral order dependence while the right - cutoff dependence.

At the photon's energy 30 MeV the chiral dependance is relatively weak: at the maximum point ($E_p \simeq 3.8$ MeV) the relative difference varies between 12 % and 28 % at LO for different angles. This difference decreases with each subsequent order resulting in 0.15 % at N^4LO+ . At the energy $E_\gamma = 100$ MeV truncation errors are larger: at the $E_p \simeq 1.46$ MeV the discrepancy is around 40 % (NLO), 15 % (N2LO), coming to 1.5 % at N^4LO+ .

The cutoff uncertainty at $E_\gamma = 30$ MeV is around 2 % and at $E_\gamma = 100$ MeV is around 8 % for all angles and at the same values of E_p as regarded above.

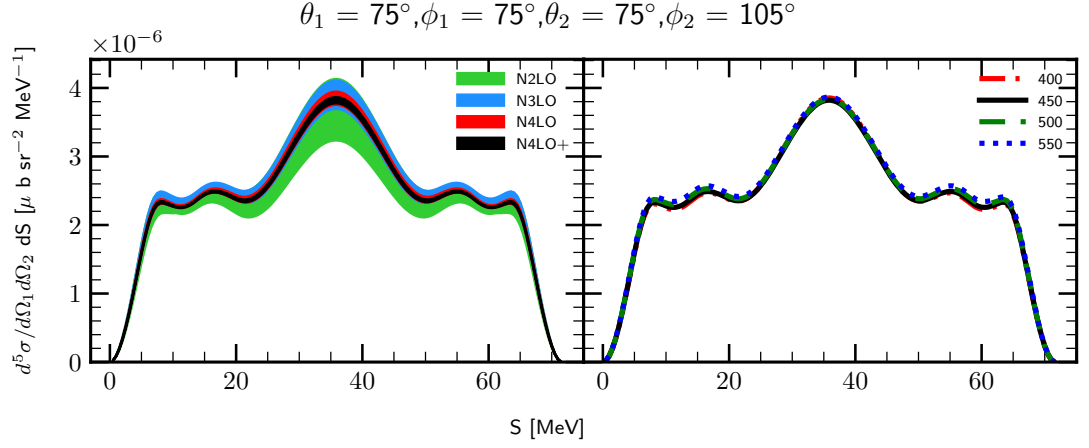


Figure 3.29: The same as on the Fig. 3.28 but with three-nucleon force.

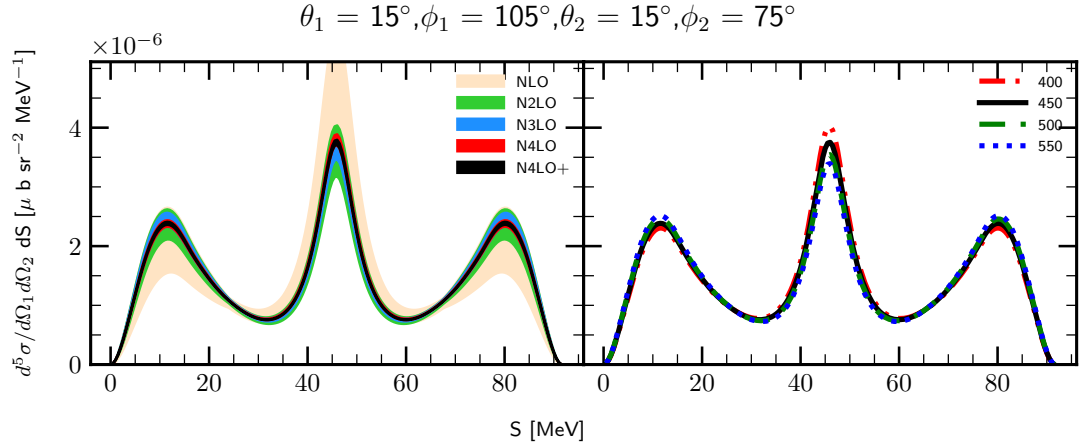


Figure 3.30: The same as on the Fig. 3.28 but for the different kinematic configuration.

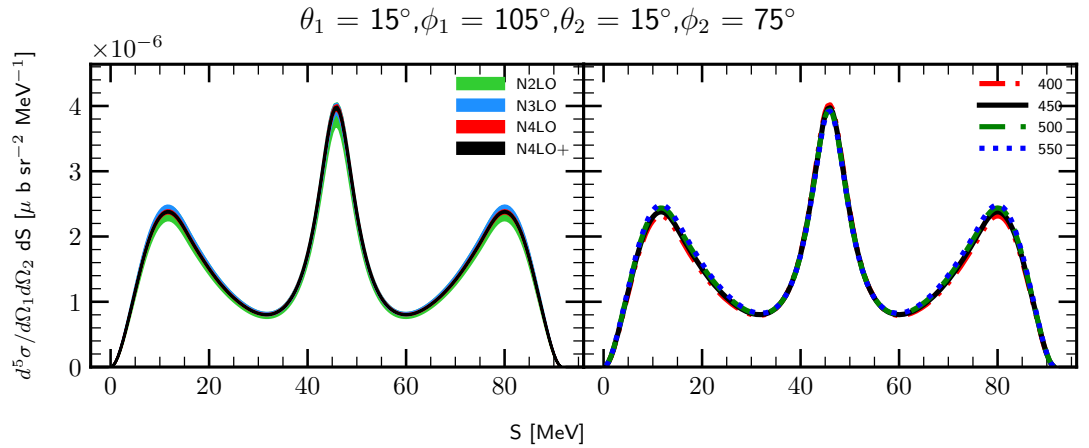


Figure 3.31: The same as on the Fig. 3.30 but but with three-nucleon force.

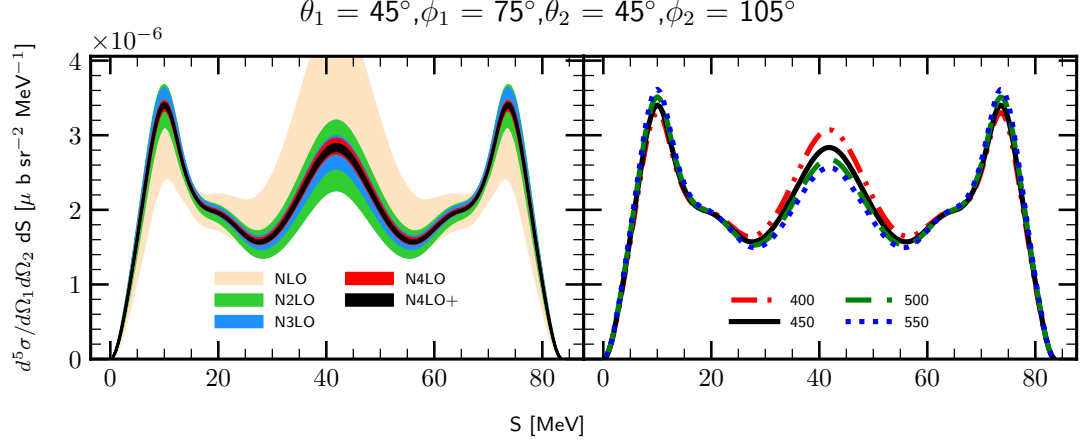


Figure 3.32: The same as on the Fig. 3.30 but for the different kinematic configuration.

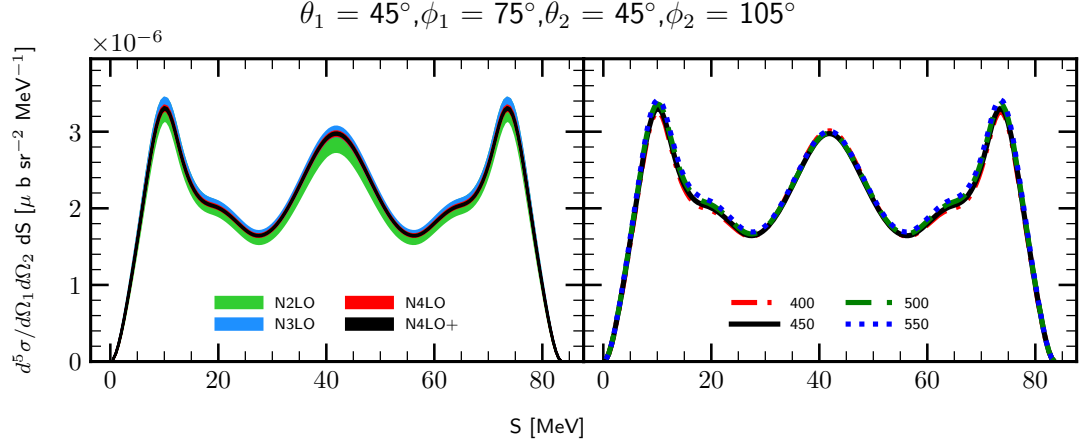


Figure 3.33: The same as on the Fig. 3.32 but but with three-nucleon force.

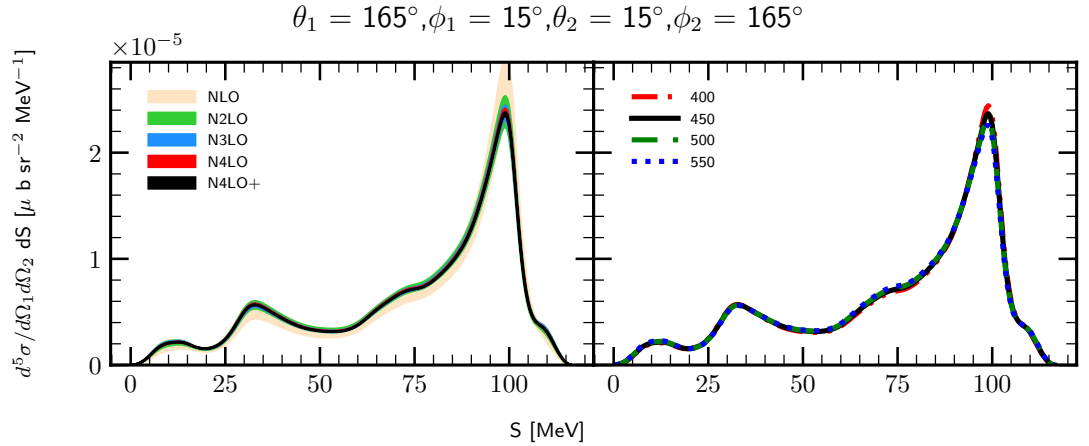


Figure 3.34: The same as on the Fig. 3.32 but for the different kinematic configuration.

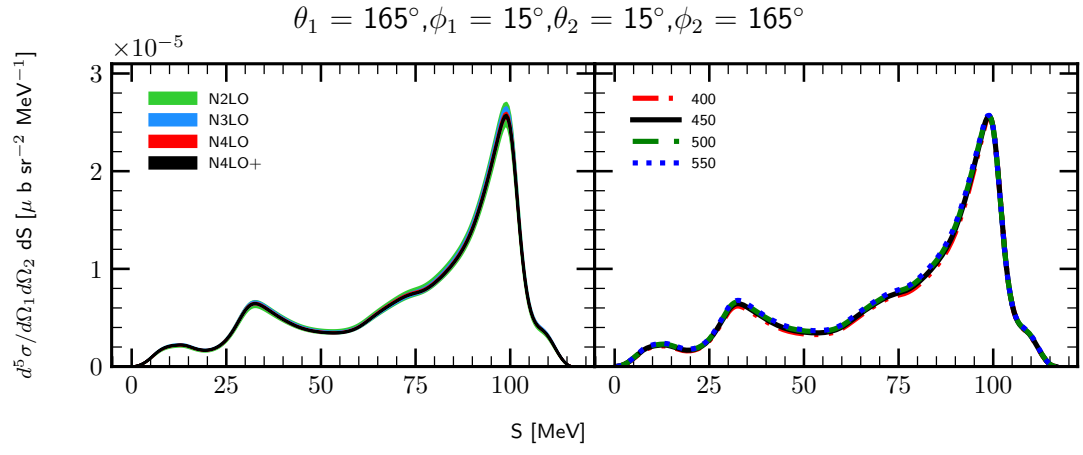


Figure 3.35: The same as on the Fig. 3.34 but but with three-nucleon force.

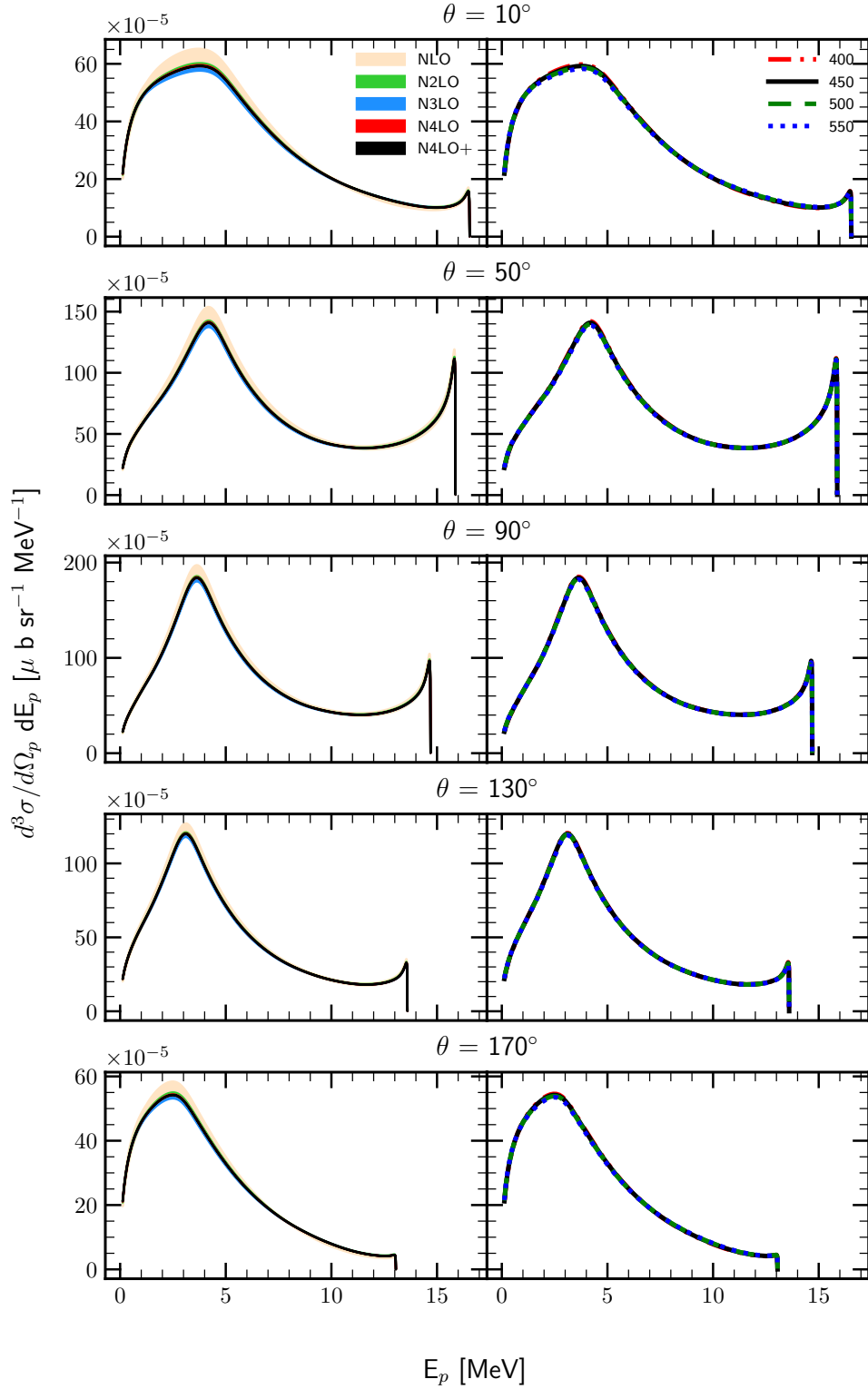
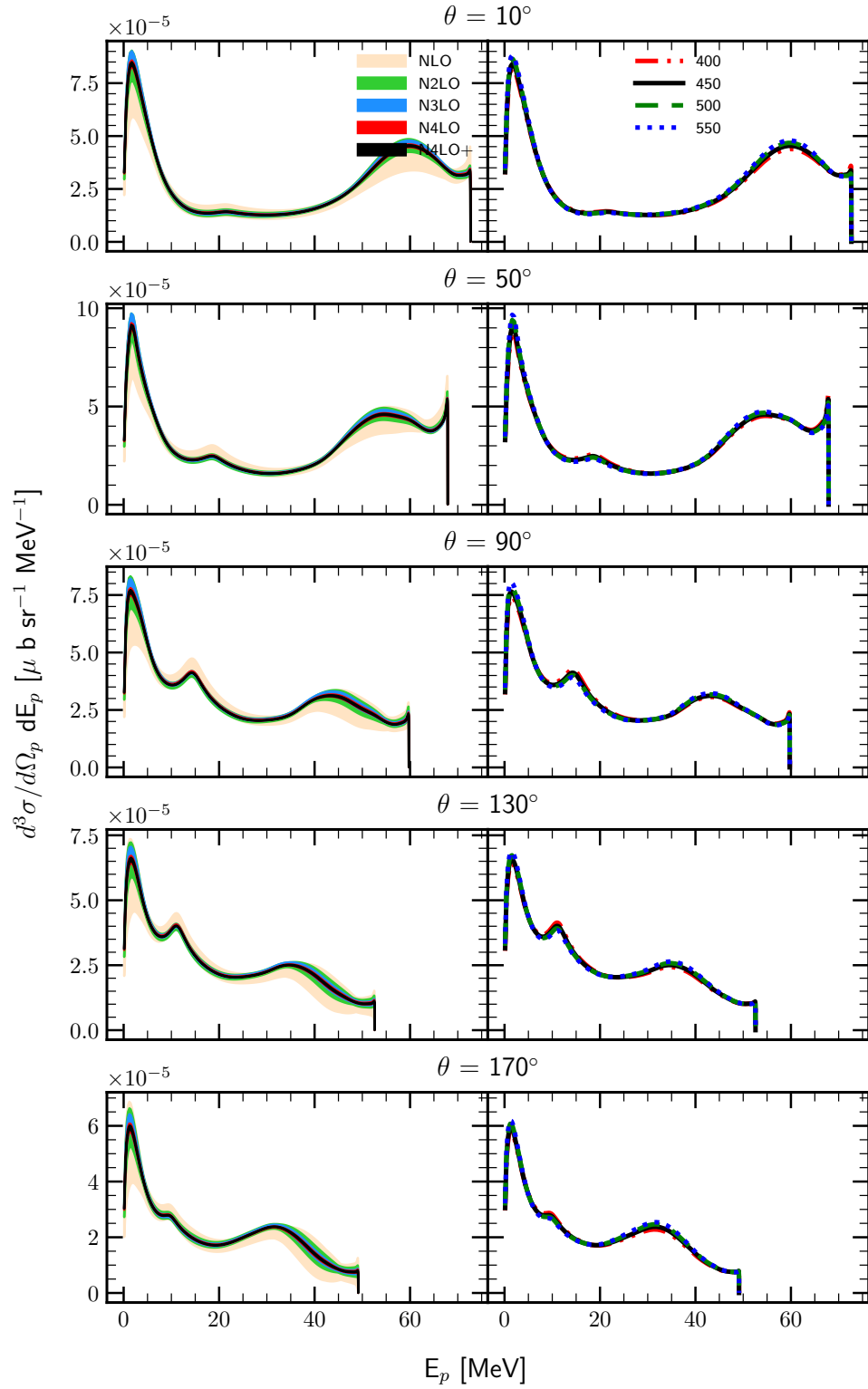


Figure 3.36: The semi-inclusive differential cross section $\frac{d^3\sigma}{d\Omega_p dE_p}$ at $E_\gamma = 30$ MeV as a function of outgoing proton's energy E_p . Each row represent predictions for different values of the outgoing proton's angle θ_p : 10°, 50°, 90°, 130° and 170°. Each column has similar lines and bands definitions as it was for exclusive cross section. Predictions have been obtained without 3NF.


 Figure 3.37: The same as on Fig. 3.36 but for $E_\gamma = 100$ MeV

3.2.2 D-n photodisintegration

The differential cross section $d\sigma/d\Omega_d$ for the ${}^3\text{He} + \gamma \rightarrow d + n$ reaction is presented on the Fig. 3.38 (for the photon's energy $E_\gamma = 30$ MeV) and on the Fig. 3.39 (for the photon's energy $E_\gamma = 100$ MeV). We see that both truncation and cutoff uncertainties are larger with increasing photon's energy. The relative spread of the truncation error at the maximum point ($\theta_p = 105^\circ$) for the lower energy is 0.05 % at N⁴LO+, while for the larger energy similar spread is 0.45 % (at N⁴LO+, $\theta_p = 120^\circ$).

The cutoff dependance is also stronger for the larger energy: it is 1.45 % at 30 MeV and 4.01 % at 100 MeV (at the points of maximum).

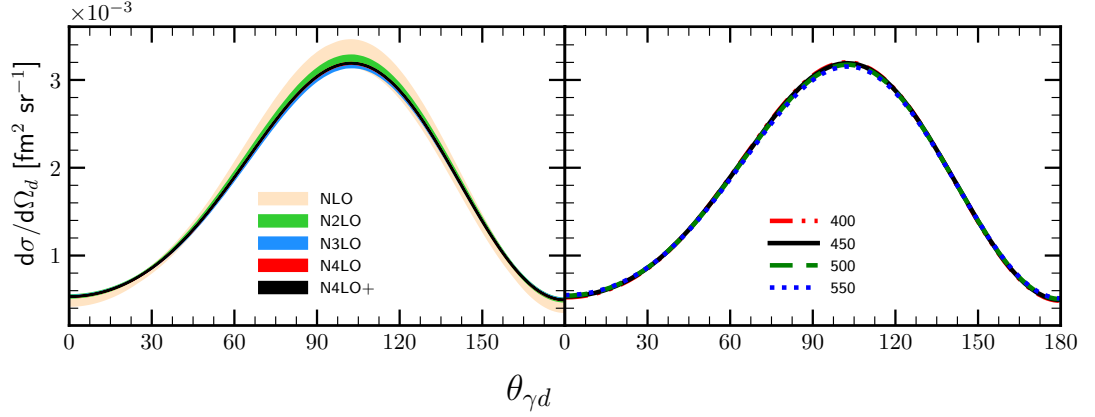


Figure 3.38: Differential cross section for the d-*n* two-body photodisintegration of ${}^3\text{He}$ as a function of the $d\gamma$ angle. The initial photon energy $E_\gamma = 30$ MeV.

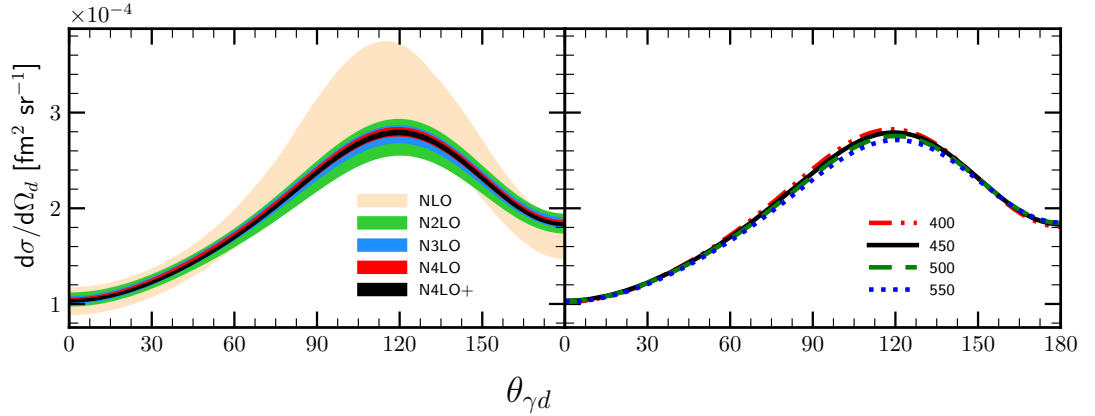


Figure 3.39: The same as on Fig. 3.38 but for the photon energy $E_\gamma = 100$ MeV

3.3 Pion absorption from the lowest atomic orbital

3.3.1 Pion absorption in ^3He

in Fig. 3.40 and 3.41 the pion absorption rates are presented as a function of the chiral order with different values of the cutoff parameter (for $\pi^- + ^3\text{He} \rightarrow p + n + n$ and $\pi^- + ^3\text{He} \rightarrow n + d$ reactions, respectively). Both figures show that with fixed chiral order the arrangement of values with respect of the cutoff parameter remains the same, namely with increasing Λ , absorption rate decreases. The only exception in both cases appears at N³LO where prediction with $\Lambda = 550$ MeV goes above other predictions. At the next order, N⁴LO, it corrects to the normal arrangement. This behavior may be connected to the 3NF used for the calculation and in order to check that I show a similar figure for a proton radius r_p in Fig. 3.42 calculated with and without 3NF (left and right panels respectively). Results obtained with 3NF show similar deviation at N³LO while data obtained without 3NF does not have that. Nevertheless, the spread of predictions with respect to the cutoff values is much smaller with 3NF and deviation seems to be not crucial as total difference between predictions in this case is very small.

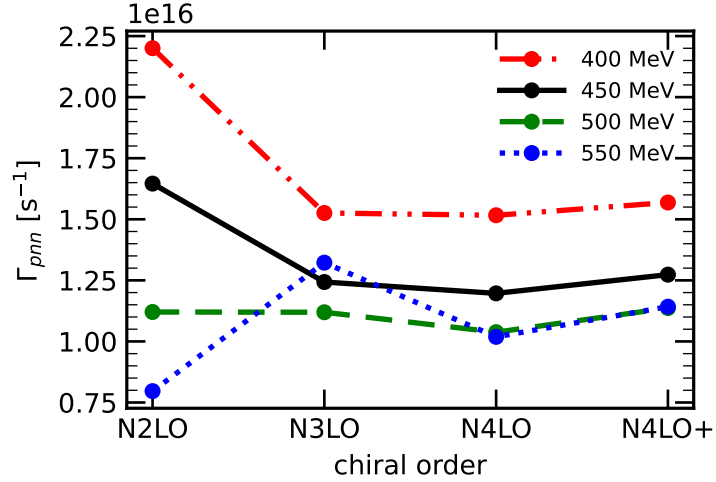


Figure 3.40: Absorption rate for $\pi^- + ^3\text{He} \rightarrow p + n + n$ reaction as a function of the chiral order with different values of the cutoff parameter Λ . Predictions were obtained with 3NF.

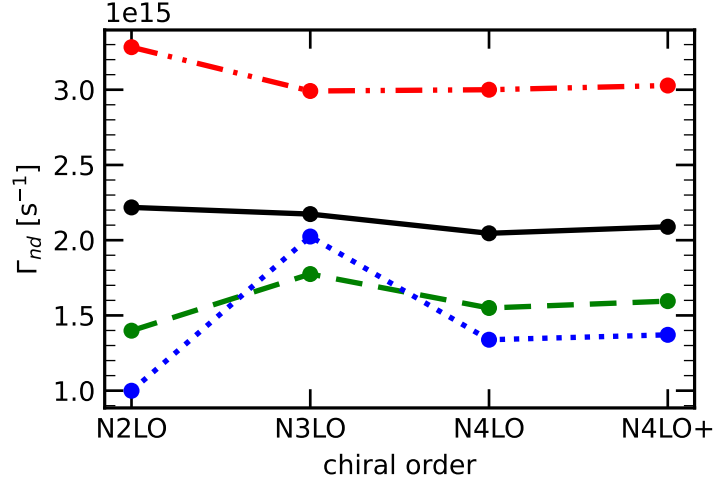
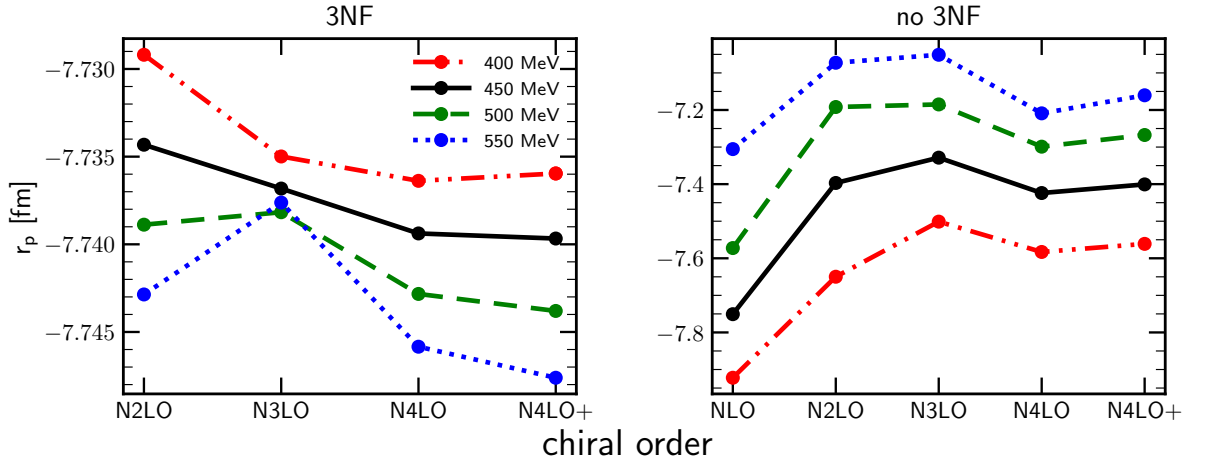
In Figs. 3.44 and 3.43 I show intensity plots for the double differential absorption rates $d^2\Gamma_{pnn}/dE_1dE_2$ for the $\pi^- + ^3\text{He} \rightarrow p + n + n$ process as functions of the nucleons energies (first nucleon is proton) and of *correct naming* Dalitz coordinates (x and y) respectively.

In Fig. 3.43 coordinates x and y are defined as:

$$\begin{aligned} x &= 3(E_1 + 2E_2 - E)/E, \\ y &= (3E_1 - E)/E, \end{aligned} \quad (3.3)$$

taking the region where $r^2 \equiv x^2 + y^2 \leq 1$.

Each of two figures consists of four panels representing predictions obtained with different values of the cutoff parameter Λ . The difference between predictions which can be noticed with the naked eye - is that area of the central region (corresponding to


 Figure 3.41: The same as in Fig. 3.40, but for $\pi^- + {}^3\text{He} \rightarrow n + d$ reaction.

 Figure 3.42: *check mt3* Proton radius r_p as a function of the chiral order calculated with different values of the cutoff parameter Λ . The radius was calculated with 2NF and 3NF (left panel) and with 2NF only (right panel).

smallest values) becomes larger with increasing Λ . It coheres to what we saw on Fig. 3.40 where total absorption rate was inversely correlated with cutoff parameter. The dominant contribution comes from the region with lowest proton energy values of $E_1 \rightarrow 0$ where both neutrons have similar large values. This is a situation when proton is a spectator while both neutrons share all energy - quasi-free scattering(QFS).

Another region with high absorption rate is neutron-neutron final state interaction (FSI(nn)). It is located at high E_1 when proton gets one third part of total energy while neutrons both get one sixth.

Next I show similar colormaps but for the predictions obtained with plane wave component only (without rescattering part) in Figs. 3.46 and 3.45. Presented plots show that the difference of predictions obtained without rescattering part with full is very large. Predicted values are few times larger and the distribution is completely different. The FSI(nn) region is not presented here in a sense that there is no peak with respect to other values. The QFS region is, on the contrary, It obviously tells us that one has to take into

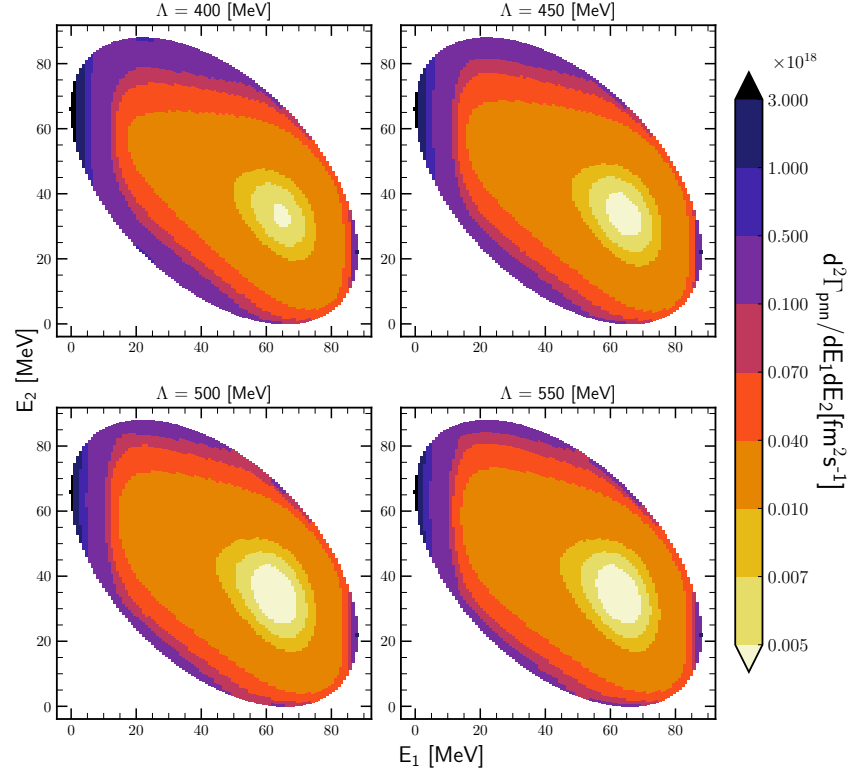


Figure 3.43: Intensity plots for the double differential absorption rates $d^2\Gamma_{pn}/dE_1 dE_2$ for the $\pi^- + {}^3\text{He} \rightarrow p + n + n$ process, obtained using the SMS potential at N⁴LO+ with all contributions possible: plane wave + rescattering, SN + 2N, 2NF+3NF. Each panel present predictions obtained with different values of the cutoff parameter Λ : from 400 MeV (upper left) to 550 MeV (lower right). Nucleon 1 is a proton.

account rescattering pat in order to obtain relevant results.

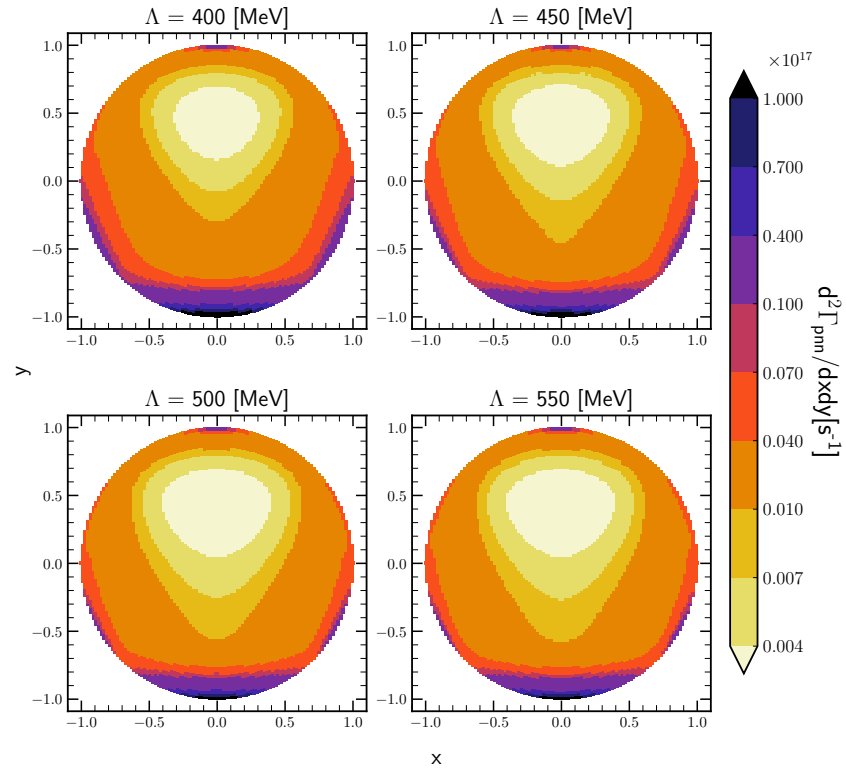


Figure 3.44: The same as in Fig. 3.44 but for the double differential absorption rates $d^2\Gamma_{pn}/dx dy$.

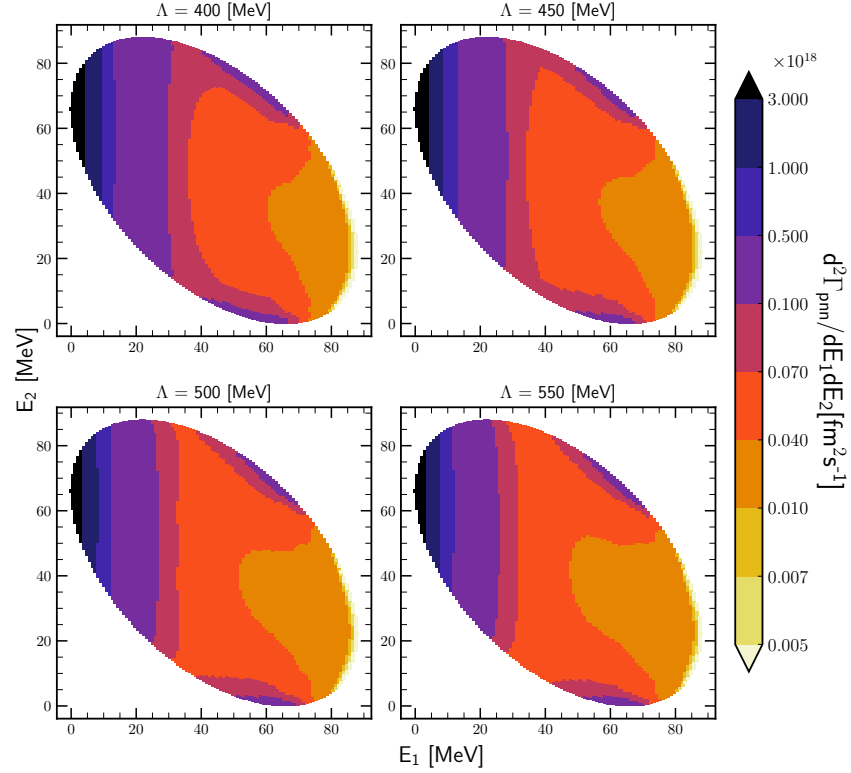


Figure 3.45: Intensity plots for the double differential absorption rates $d^2\Gamma_{pn}/dE_1 dE_2$ for the $\pi^- + {}^3\text{He} \rightarrow p + n + n$ process, obtained using the SMS potential at N⁴LO+ with plane wave part only (without rescattering). All other contributions are the same as in Fig. 3.44: SN + 2N and 2NF+3NF. Each panel present predictions obtained with different values of the cutoff parameter Λ : from 400 MeV (upper left) to 550 MeV (lower right). Nucleon 1 is a proton.

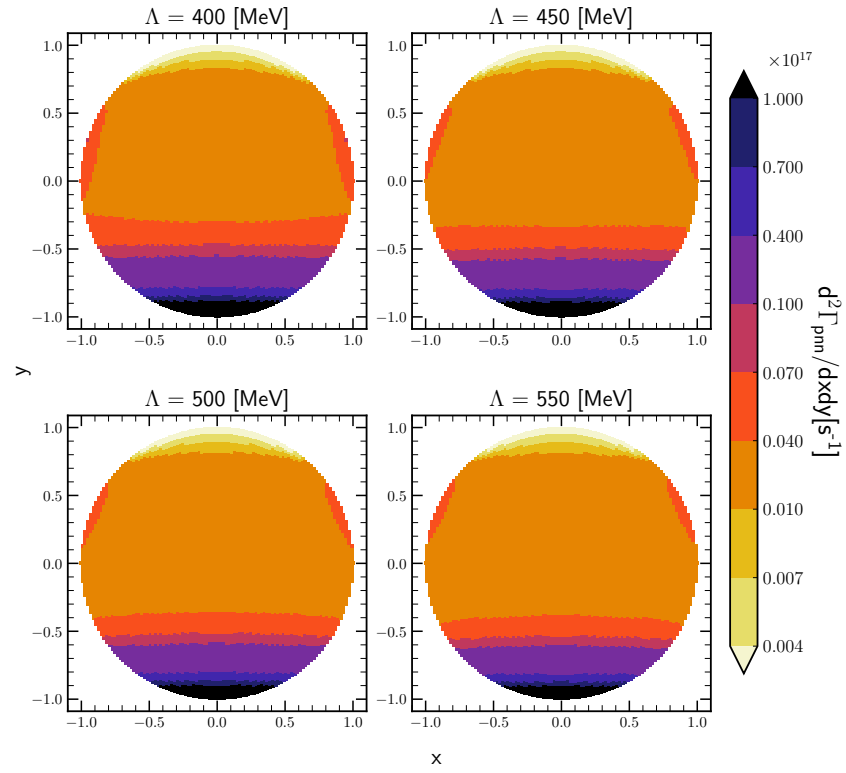


Figure 3.46: The same as in Fig. 3.46 but for the double differential absorption rates $d^2\Gamma_{pnn}/dxdy$.

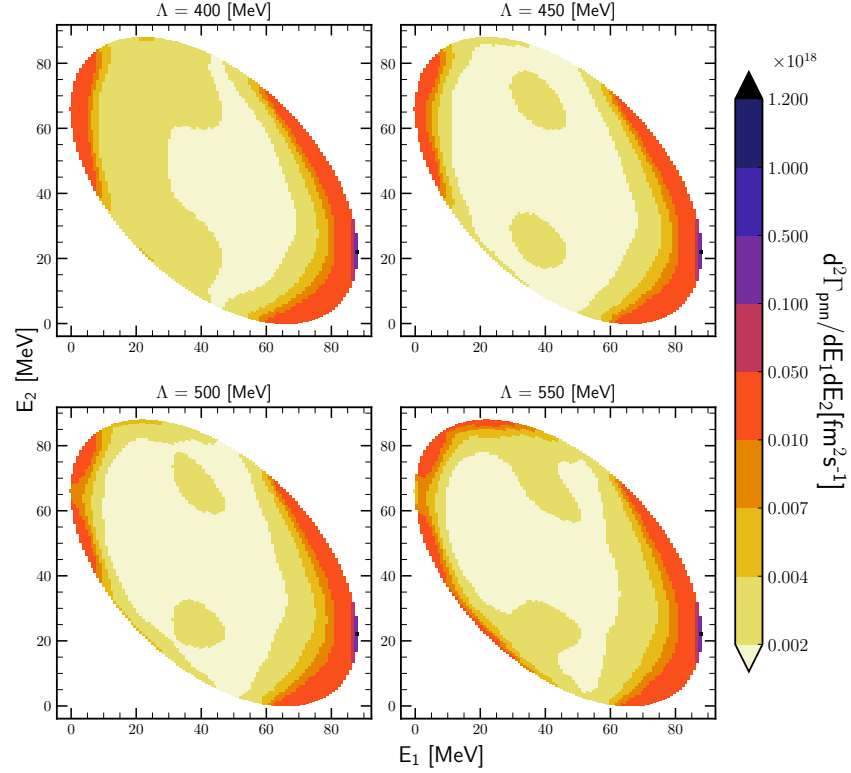


Figure 3.47: Intensity plots for the double differential absorption rates $d^2\Gamma_{pn}/dE_1 dE_2$ for the $\pi^- + {}^3\text{He} \rightarrow p + n + n$ process, obtained using the SMS potential at N⁴LO+ with SN current only (without 2N). All other contributions are the same as in Fig. 3.44: PWIAS+RESC and 2NF+3NF. Each panel present predictions obtained with different values of the cutoff parameter Λ : from 400 MeV (upper left) to 550 MeV (lower right). Nucleon 1 is a proton.

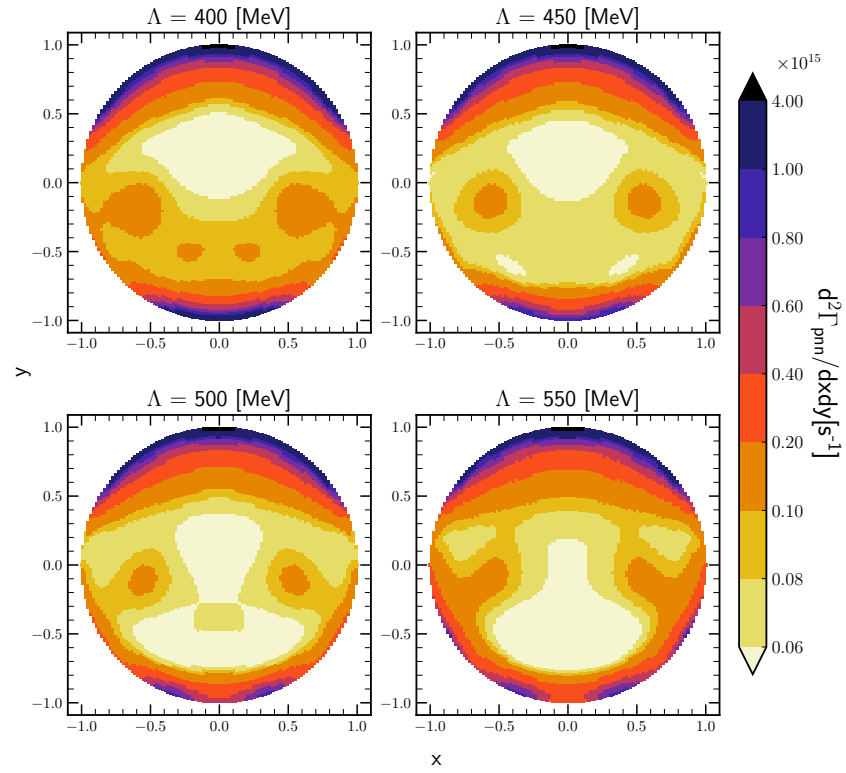


Figure 3.48: The same as in Fig. 3.48 but for the double differential absorption rates $d^2\Gamma_{pnn}/dx dy$.

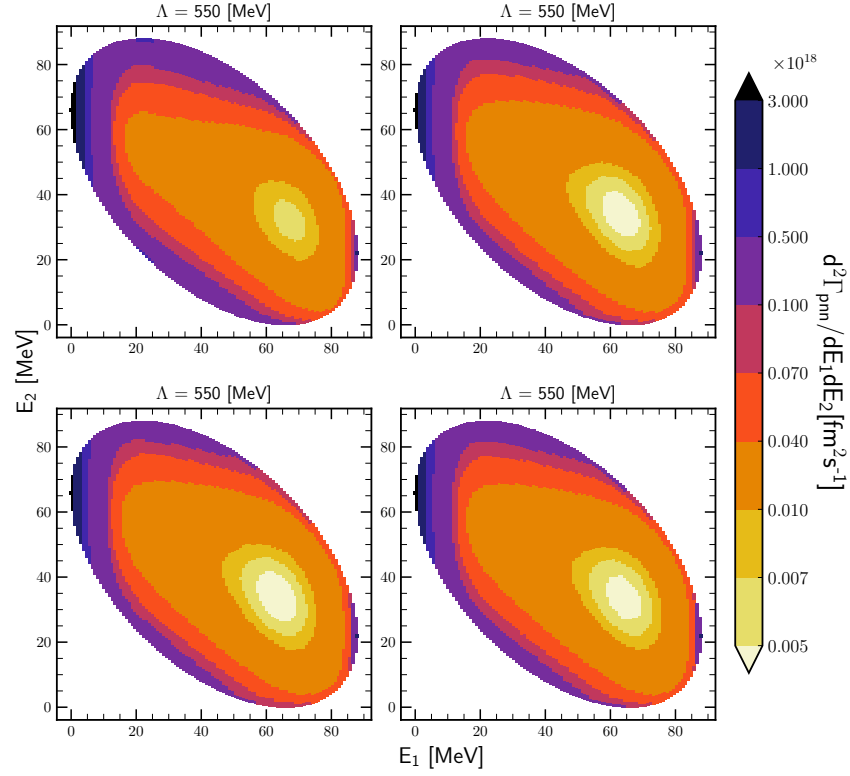


Figure 3.49: Intensity plots for the double differential absorption rates $d^2\Gamma_{pn}/dE_1 dE_2$ for the $\pi^- + {}^3\text{He} \rightarrow p + n + n$ process, obtained using the SMS potential at N⁴LO+ with all contributions possible: plane wave + rescattering, SN + 2N, 2NF+3NF. Each panel present predictions obtained with different chiral orders: from N²LO (upper left) to N⁴LO+ (lower right). Nucleon 1 is a proton.

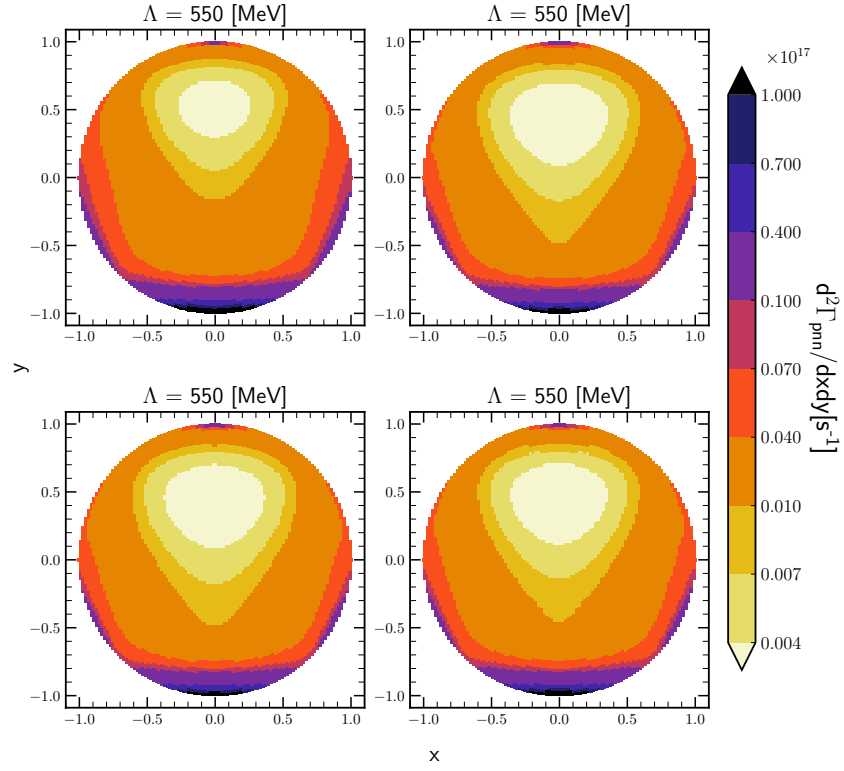


Figure 3.50: The same as in Fig. 3.50 but for the double differential absorption rates $d^2\Gamma_{pnn}/dxdy$.

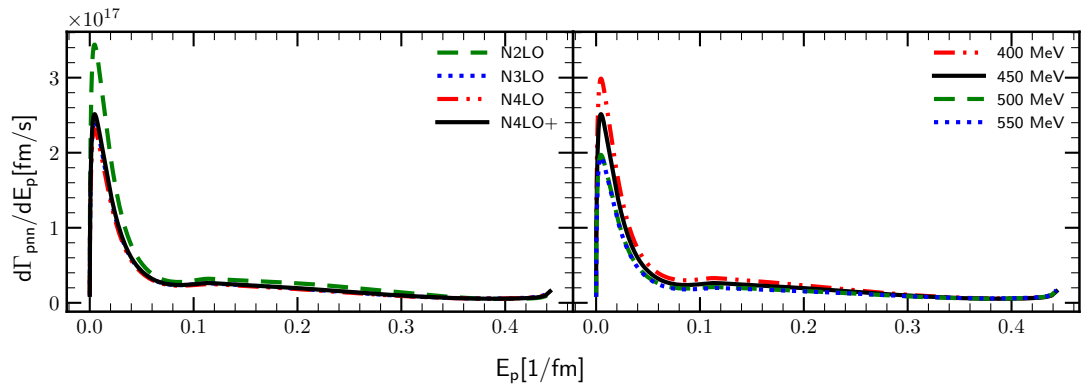


Figure 3.51

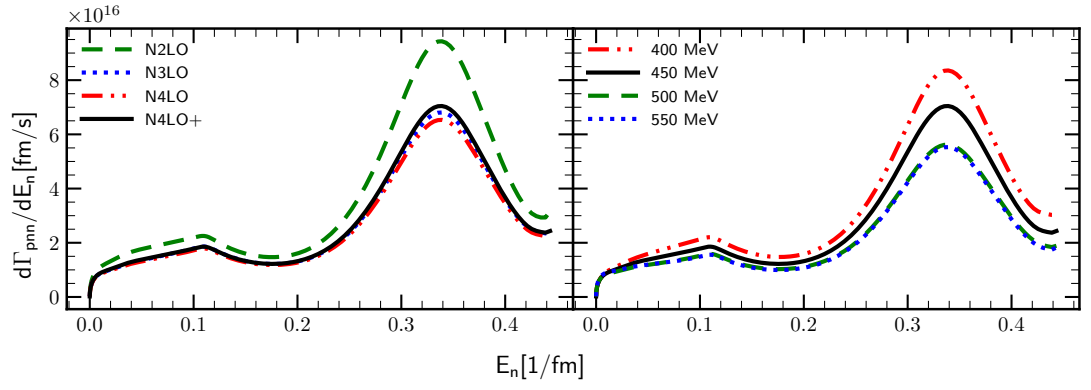


Figure 3.52

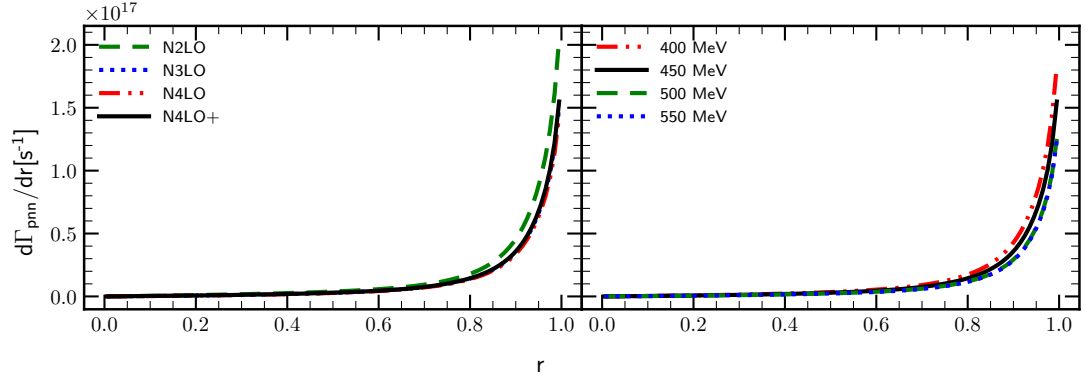


Figure 3.53

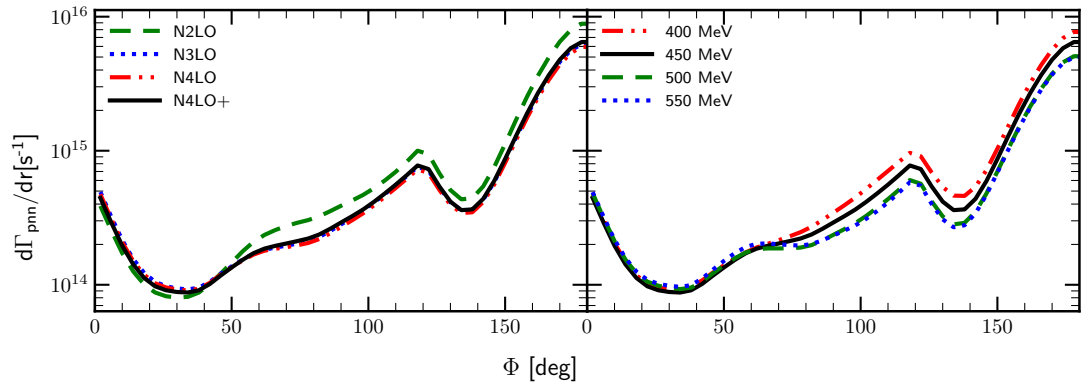


Figure 3.54

3.3.2 $\pi^- + {}^3\text{H} \rightarrow n + n + n$

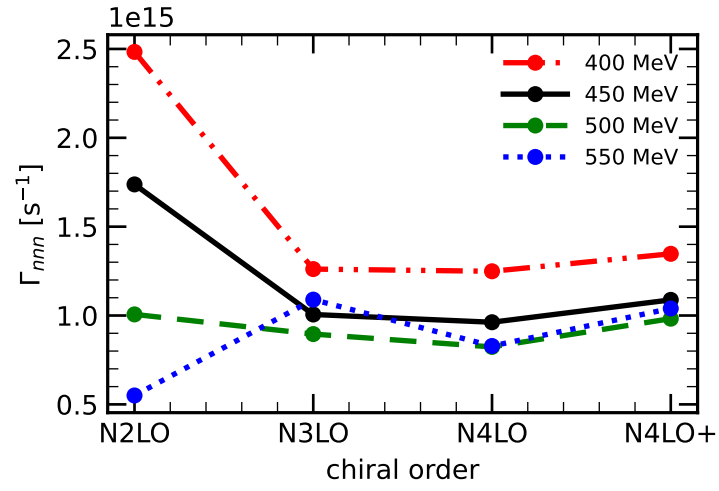


Figure 3.55

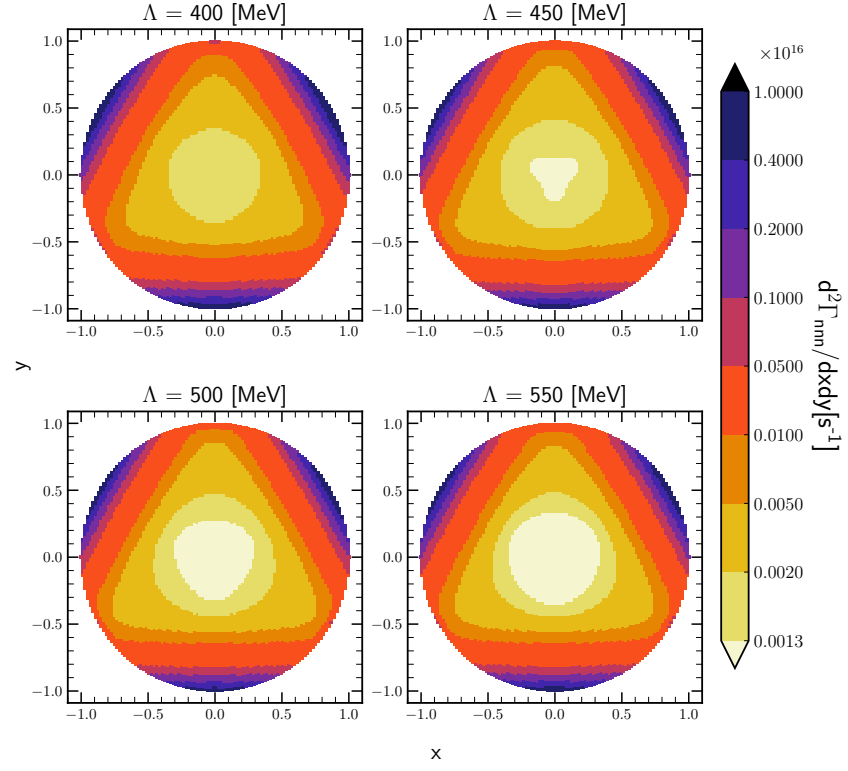


Figure 3.56

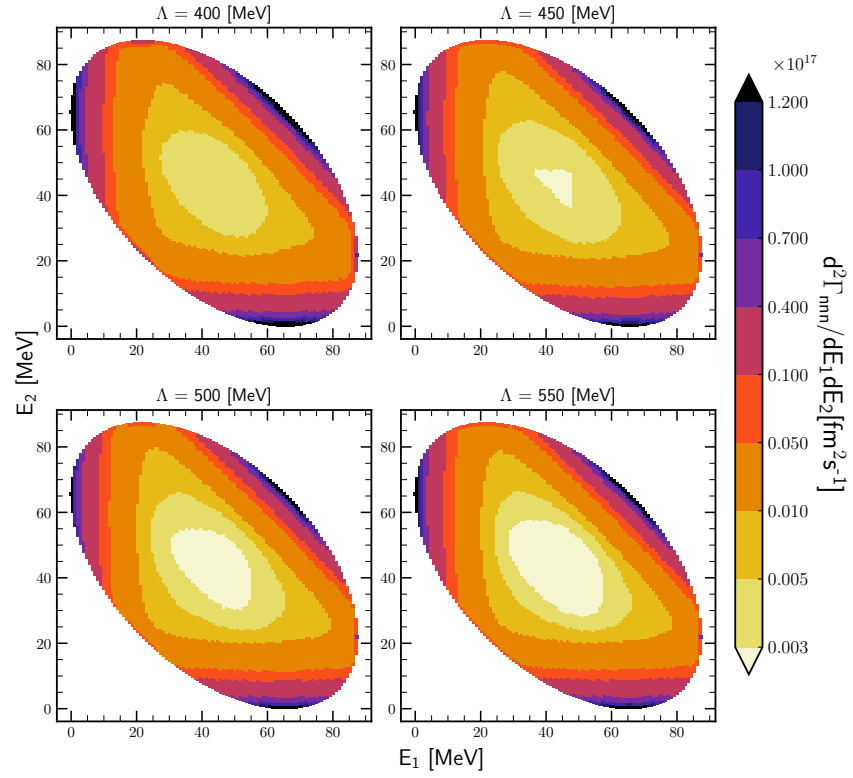


Figure 3.57

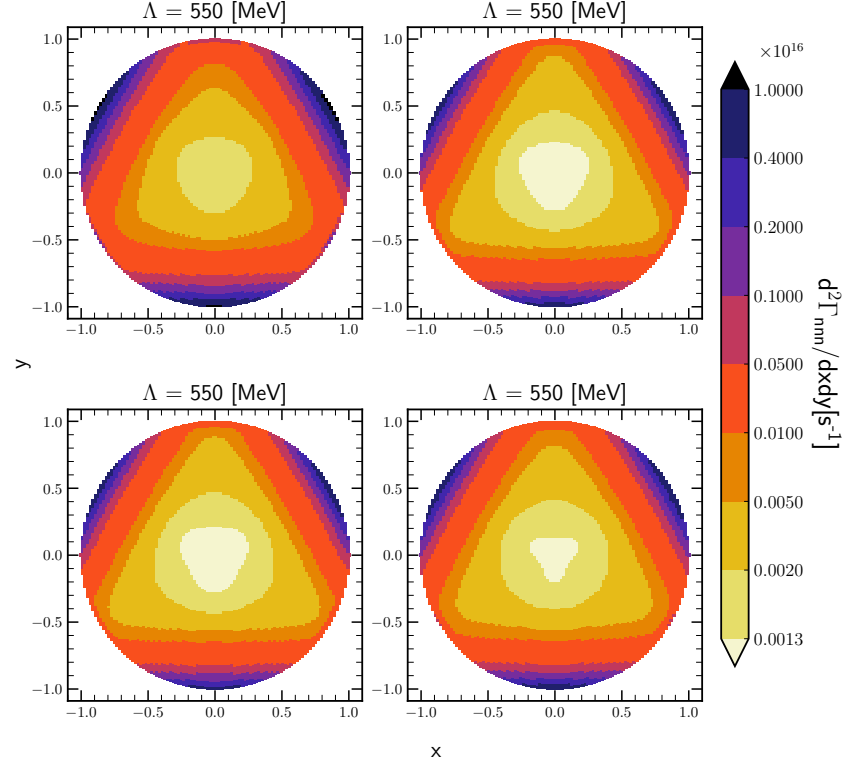


Figure 3.58

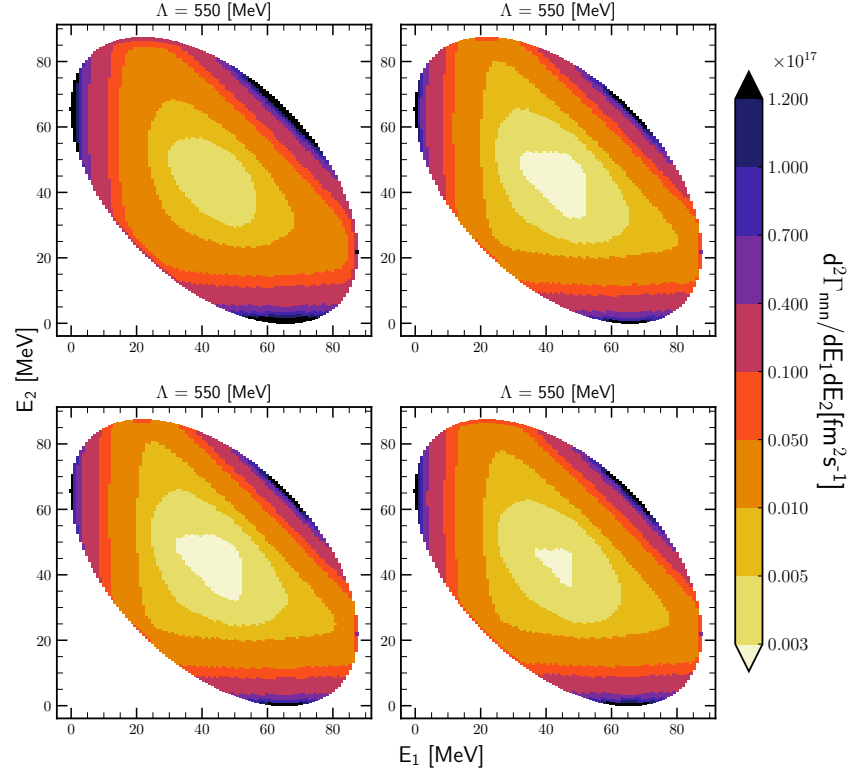


Figure 3.59

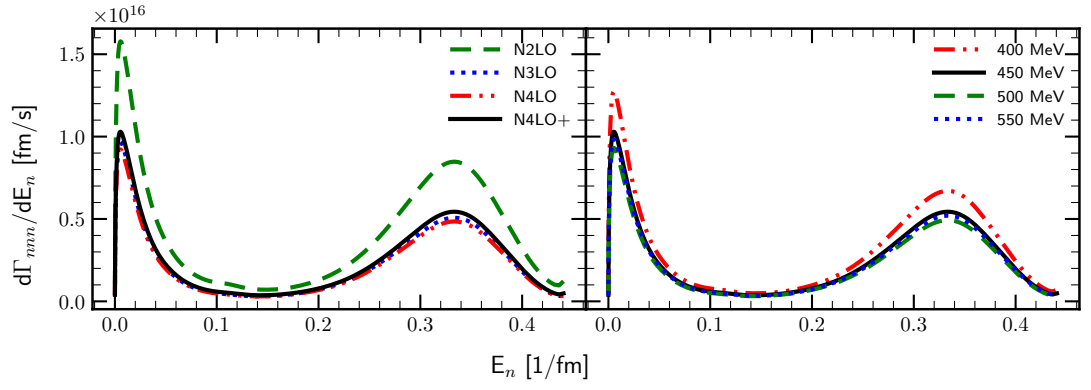


Figure 3.60

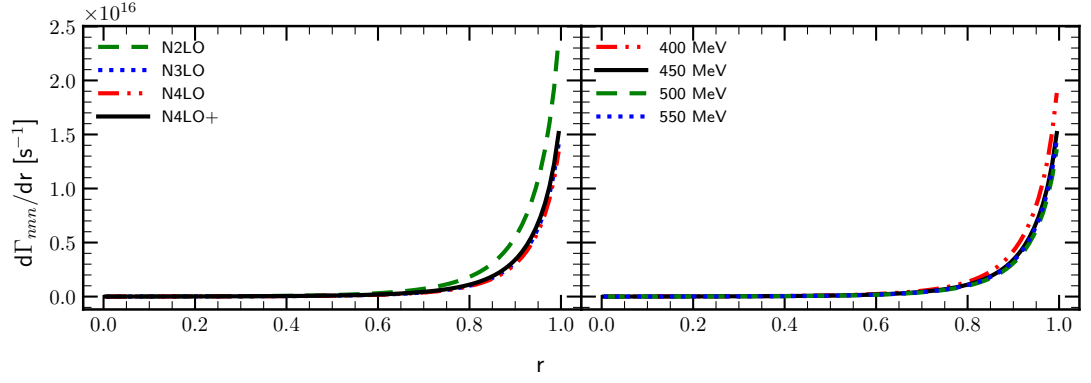


Figure 3.61

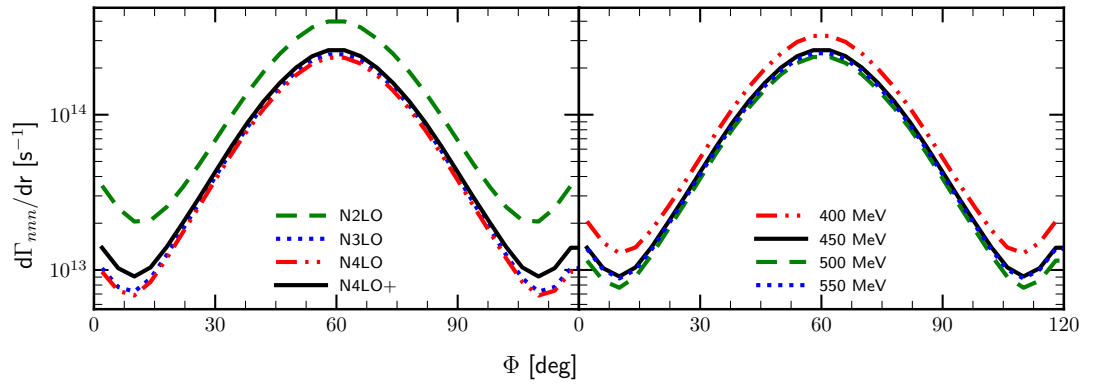


Figure 3.62

BIBLIOGRAPHY

- [1] B.L. Ioffe. Qcd (quantum chromodynamics) at low energies. *Progress in Particle and Nuclear Physics*, 56(1):232–277, 2006.
- [2] W. Glöckle. Effects of the two-pion exchange three-nucleon force in the triton and ^3He . *Nuclear Physics A*, 381(3):343–364, 1982.
- [3] V. G. J. Stoks, R. A. M. Klomp, C. P. F. Terheggen, and J. J. de Swart. Construction of high-quality nn potential models. *Phys. Rev. C*, 49:2950–2962, Jun 1994.
- [4] R. B. Wiringa, V. G. J. Stoks, and R. Schiavilla. Accurate nucleon-nucleon potential with charge-independence breaking. *Phys. Rev. C*, 51:38–51, Jan 1995.
- [5] A. Nogga, H. Kamada, and W. Glöckle. Modern nuclear force predictions for the α particle. *Phys. Rev. Lett.*, 85:944–947, Jul 2000.
- [6] H Arenhövel and M. Sanzone. Photodisintegration of the deuteron: A Review of theory and experiment. *Few Body Syst. Suppl.*, 3:1–183, 1991.
- [7] Robert B. Wiringa, V. G. J. Stoks, and R. Schiavilla. An Accurate nucleon-nucleon potential with charge independence breaking. *Phys. Rev.*, C51:38–51, 1995.
- [8] V. G. J. Stoks, R. A. M. Klomp, M. C. M. Rentmeester, and J. J. de Swart. Partial-wave analysis of all nucleon-nucleon scattering data below 350 mev. *Phys. Rev. C*, 48:792–815, Aug 1993.
- [9] Steven Weinberg. Nuclear forces from chiral lagrangians. *Physics Letters B*, 251(2):288–292, 1990.
- [10] Steven Weinberg. Effective chiral lagrangians for nucleon-pion interactions and nuclear forces. *Nuclear Physics B*, 363(1):3–18, 1991.
- [11] R. Machleidt and D. R. Entem. Chiral effective field theory and nuclear forces. *Phys. Rept.*, 503:1–75, 2011.
- [12] Evgeny Epelbaum. Few-nucleon forces and systems in chiral effective field theory. *Progress in Particle and Nuclear Physics*, 57(2):654–741, 2006.

- [13] M. Piarulli, L. Girlanda, L. E. Marcucci, S. Pastore, R. Schiavilla, and M. Viviani. Electromagnetic structure of $A = 2$ and 3 nuclei in chiral effective field theory. *Phys. Rev.*, C87(1):014006, 2013.
- [14] M. Piarulli, L. Girlanda, R. Schiavilla, R. Navarro Pérez, J. E. Amaro, and E. Ruiz Arriola. Minimally nonlocal nucleon-nucleon potentials with chiral two-pion exchange including Δ resonances. *Phys. Rev. C*, 91:024003, Feb 2015.
- [15] E. Epelbaum, H. Krebs, and U. G. Meißner. Precision nucleon-nucleon potential at fifth order in the chiral expansion. *Phys. Rev. Lett.*, 115(12):122301, 2015.
- [16] P. Reinert, H. Krebs, and E. Epelbaum. Semilocal momentum-space regularized chiral two-nucleon potentials up to fifth order. *Eur. Phys. J.*, A54(5):86, 2018.
- [17] Carl Gustav Jakob Jacobi. Ueber gauss neue methode, die werthe der integrale näherungsweise zu finden. 1826.
- [18] C. Van Der Leun and C. Alderliesten. The deuteron binding energy. *Nuclear Physics A*, 380(2):261–269, 1982.
- [19] Jun John Sakurai. *Modern quantum mechanics; rev. ed.* Addison-Wesley, Reading, MA, 1994.
- [20] E Epelbaum, H Krebs, and Ulf-G Meißner. Precision nucleon-nucleon potential at fifth order in the chiral expansion. *Phys. Rev. Lett.*, 115(12):122301, 2015.
- [21] E Epelbaum, H Krebs, and U-G Meißner. Improved chiral nucleon-nucleon potential up to next-to-next-to-next-to-leading order. *Eur. Phys. J. A*, 51(5), May 2015.
- [22] S. Binder et al. Few-nucleon systems with state-of-the-art chiral nucleon-nucleon forces. *Phys. Rev.*, C93(4):044002, 2016.
- [23] Evgeny Epelbaum. High-precision nuclear forces : Where do we stand? *PoS*, CD2018:006, 2020.
- [24] Sean B. S. Miller, Andreas Ekström, and Christian Forssén. Posterior predictive distributions of neutron-deuteron cross sections, 2022.
- [25] M. Bosman, A. Bol, J.F. Gilot, P. Leleux, P. Lipnik, and P. Macq. Measurement of the total cross section for the $^1\text{H}(n, \gamma) ^2\text{H}$ reaction between 37 and 72 mev. *Physics Letters B*, 82(2):212–215, 1979.
- [26] J. Arends, H.J. Gassen, A. Hegerath, B. Mecking, G. Nöldeke, P. Prenzel, T. Reichelt, A. Voswinkel, and W.W. Sapp. Experimental investigation of deuteron photodisintegration in the δ -resonance region. *Nuclear Physics A*, 412(3):509–522, 1984.
- [27] D. M. Skopik, Y. M. Shin, M. C. Phenneger, and J. J. Murphy. Photodisintegration of deuterium determined from the electrodisintegration process. *Phys. Rev. C*, 9:531–536, Feb 1974.
- [28] R. Moreh, T. J. Kennett, and W. V. Prestwich. $^2\text{H}(\gamma, n)$ absolute cross section at 2754 kev. *Phys. Rev. C*, 39:1247–1250, Apr 1989.

- [29] Y. Birenbaum, S. Kahane, and R. Moreh. Absolute cross section for the photodisintegration of deuterium. *Phys. Rev. C*, 32:1825–1829, Dec 1985.
- [30] R. Bernabei, A. Incicchitti, M. Mattioli, P. Picozza, D. Prosperi, L. Casano, S. d’Angelo, M. P. De Pascale, C. Schaerf, G. Giordano, G. Matone, S. Frullani, and B. Girolami. Total cross section for deuteron photodisintegration between 15 and 75 mev. *Phys. Rev. Lett.*, 57:1542–1545, Sep 1986.
- [31] I. A. Rachek, L. M. Barkov, S. L. Belostotsky, V. F. Dmitriev, M. V. Dyug, R. Gilman, R. J. Holt, B. A. Lazarenko, S. I. Mishnev, V. V. Nelyubin, D. M. Nikolenko, A. V. Osipov, D. H. Potterveld, R. Sh. Sadykov, Yu. V. Shestakov, V. N. Stibunov, D. K. Toporkov, H. de Vries, and S. A. Zevakov. Measurement of tensor analyzing powers in deuteron photodisintegration. *Phys. Rev. Lett.*, 98:182303, May 2007.
- [32] S. Q. Ying, E. M. Henley, and G. A. Miller. DEUTERON PHOTODISINTEGRATION. *Phys. Rev.*, C38:1584–1600, 1988. including references.
- [33] E. De Sanctis et al. Deuteron Photodisintegration Cross-section Between 100-MeV and 220-MeV. *Phys. Rev. Lett.*, 54:1639, 1985.
- [34] S.I. Mishnev, D.M. Nikolenko, S.G. Popov, I.A. Rachek, A.B. Temnykh, D.K. Toporkov, E.P. Tsentalovich, B.B. Wojtsekhowski, S.L. Belostotsky, V.V. Nelyubin, V.V. Sulimov, and V.N. Stibunov. Measurement of the analyzing power components in photodisintegration of the polarized deuteron. *Physics Letters B*, 302(1):23–28, 1993.
- [35] K M Schmitt and H Arenhövel. Deuteron photodisintegration with the bonn OBE potentials. *Few-body syst.*, 7(3):95–117, 1989.
- [36] W. Del Bianco, L. Federici, G. Giordano, G. Matone, G. Pasquariello, P. Picozza, R. Caloi, L. Casano, M. P. De Pascale, L. Ingrosso, M. Mattioli, E. Poldi, C. Schaerf, P. Pelfer, D. Prosperi, S. Frullani, B. Girolami, and H. Jeremie. Neutron asymmetry measurements in the deuteron photodisintegration between 10 and 70 mev. *Phys. Rev. Lett.*, 47:1118–1120, Oct 1981.
- [37] M. P. De Pascale, G. Giordano, G. Matone, D. Babusci, R. Bernabei, O. M. Bilaniuk, L. Casano, S. d’Angelo, M. Mattioli, P. Picozza, D. Prosperi, C. Schaerf, S. Frullani, and B. Girolami. Polarization asymmetry in the photodisintegration of the deuteron. *Phys. Rev. C*, 32:1830–1841, Dec 1985.
- [38] K.-H. Krause, J. Sobolewski, J. Ahrens, J.M. Henneberg, and B. Ziegler. Photodisintegration of the deuteron by linearly polarized photons. *Nuclear Physics A*, 549(3):387–406, 1992.
- [39] V P Barannik, V G Gorbenko, V A Gushchin, Y V Zhebrovskii, L Y Kolesnikov, Y V Kulish, A L Rubashkin, and P V Sorokin. Study of the cross-section asymmetry in photodisintegration of the deuteron by polarized. gamma. rays at low energies. *Sov. J. Nucl. Phys. (Engl. Transl.); (United States)*, 38:5, 11 1983.
- [40] I E Vnukov, I V Glavanakov, Y F Krechetov, A P Potylitsyn, G A Saruev, V N Stibunov, and A N Tabachenko. Photodisintegration of the deuteron by linearly

- polarized photons below the pion-production threshold. *Sov. J. Nucl. Phys. (Engl. Transl.); (United States)*, 47:4, 4 1988.
- [41] R. W. Jewell, W. John, J. E. Sherwood, and D. H. White. Polarization of photoneutrons produced from deuterium by 2.75-mev gamma rays. *Phys. Rev.*, 139:B71–B79, Jul 1965.
 - [42] J.M. Cameron, C.A. Davis, H. Fielding, P. Kitching, J. Pasos, J. Soukup, J. Uegaki, J. Wesick, H.S. Wilson, R. Abegg, D.A. Hutcheon, C.A. Miller, A.W. Stetz, and I.J. van Heerden. Radiative capture of polarized neutrons by hydrogen below the pion production threshold. *Nuclear Physics A*, 458(4):637–651, 1986.